Pre- and Post-entry, Descent and Landing Assessment of the Martian Atmosphere for the Mars 2020 Rover

The Planetary Science Journal, 3:147 (28pp), 2022 June https://doi.org/10.3847/PSJ/ac7148

Pre- and Post-entry, Descent and Landing Assessment of the Martian Atmosphere for the Mars 2020 Rover

Michael A. Mischna[1], Gregory Villar[1], David M. Kass[1], Soumyo Dutta[2], Scot Rafkin[3], Daniel Tyler[4], Jeffrey Barnes[4], Bruce Cantor[5], Stephen R. Lewis[6], David Hinson[7], Jorge Pla-García[8,9], Armin Kleinböhl[1], and Chris Karlgaard[10]
[1] Jet Propulsion Laboratory, California Institute of Technology, 4800 Oak Grove Drive, Pasadena, CA 91109, USA; michael.a.mischna@jpl.nasa.gov
[2] NASA Langley Research Center, 1 N. Dryden Street, M/S 489, Hampton, VA 23681, USA
[3] Southwest Research Institute, Department of Space Studies, 1050 Walnut Street, Ste. 300, Boulder, CO 80302, USA
[4] Oregon State University, College of Earth, Ocean, and Atmospheric Sciences, 104 CEOAS Admin. Bldg., Corvallis, OR 97331, USA
[5] Malin Space Science Systems, PO Box 920148, San Diego, CA 92121, USA
[6] The Open University, Walton Hall, Milton Keynes, MK7 6AA, UK
[7] SETI Institute, 189 Bernardo Avenue, Ste. 200, Mountain View, CA 94043, USA
[8] Space Science Institute, 4765 Walnut Street, Ste. B, Boulder, CO 80301, USA
[9] Centro de Astrobiología (CSIC-INTA), E-28850 Torrejon de Ardoz, Madrid, Spain
[10] Analytical Mechanics Associates, Inc., 21 Enterprise Parkway, Hampton, VA 23666, USA
Received 2021 September 17; revised 2022 May 16; accepted 2022 May 17; published 2022 June 23

Abstract

This review provides an analysis of activities undertaken by the Mars 2020 Council of Atmospheres (CoA) in support of the entry, descent, and landing (EDL) of the Mars 2020 rover Perseverance in Jezero crater, Mars. The activities of the CoA were designed to evaluate the safety of early-stage landing site candidates and, later, to constrain the range of plausible conditions expected at Jezero crater during the early northern spring season of EDL, following the successful blueprint of similar councils for prior landed Mars missions. The multiyear effort of the CoA involved using a combination of numerical modeling of the local Martian atmosphere with limited-domain mesoscale models and atmospheric reanalysis using data assimilation techniques, along with atmospheric observations from multiple orbiting assets, to generate an atmospheric "forecast" for the day of landing. Here we present an overview of these activities, focusing in greater detail on those elements that depart from prior CoA activities as performed for Mars Phoenix, Mars Science Laboratory, and the InSight lander. Following the successful landing of Perseverance on 2021 February 18, reconstruction and reassessment activities were performed and are presented here, comparing prelanding predictions with actual, as-flown conditions.

Unified Astronomy Thesaurus concepts: Mars (1007); Planetary climates (2184); Planetary atmospheres (1244); Atmospheric science (116); Planetary science (1255)

1. Introduction

The successful landing of the Perseverance rover on 2021 February 18 marked the culmination of 7 yr of effort by a team of engineers and atmospheric scientists (known informally as the Council of Atmospheres, CoA) to characterize, query, and forecast the weather conditions around Jezero crater, Mars (18.°38N, 77.°58E) in support of the activities of the Mars 2020 entry, descent, and landing (EDL) team. Unlike entry systems that follow ballistic trajectories (such as Phoenix and InSight), the Mars 2020 entry system uses hypersonic entry guidance, which increases the downrange flight distance at lower altitudes, leading to 100 km of horizontal flight at ∼15 km altitude relative to the Mars Orbiter Laser Altimeter (MOLA) reference datum, over which changes in atmospheric density can impact the flight trajectory. Following parachute deployment and before backshell separation, the spacecraft is reducing speed and at the mercy of the local wind field. It is desirable, then, to bound the physical limits of both density and wind, at a minimum, in order to optimize the performance of the entry system guidance software.

The purpose of this multiyear activity was threefold. The first part was to assess the "flyability" of the atmosphere over early candidate landing sites as selected over four Mars 2020 Landing Site Workshops (LSWs; 2014–2018). This included a high-level survey of atmospheric conditions at approximately 12 sites in order to highlight potentially problematic conditions that would produce elevated risk to successful EDL. Along with an evaluation of surface conditions (by the similarly named Council of Terrains), these environmental assessments provided initial guidance to the science community about landing site safety.

Second, once Jezero crater was selected as the Mars 2020 landing site, the goal of the CoA activities was to identify, as early as possible, any specific atmospheric risks to safe landing with respect to perturbations in atmospheric density, as well as wind speed and wind shear, that could affect the flight path of the entry system and to communicate the expected state and uncertainty of atmospheric conditions during EDL to the broader engineering team. This effort comprised the majority of CoA efforts and involved a substantial amount of modeling and data analysis work.

Third, in the weeks leading up to EDL, the CoA provided increasingly frequent assessments of near-real-time atmospheric conditions from orbital assets (including Mars Reconnaissance Orbiter, Mars Odyssey, and Mars Express) and provided updated forecasts to the EDL team to allow for last-minute adjustments to flight parameters in response to, e.g., transient dust or storm activity over Jezero crater. This final activity concluded with a final forecast just hours before the Mars 2020 landing.

The high-level structure of this effort broadly mimicked those activities performed for the Mars Science Laboratory (MSL, which landed in 2012), although there were several modifications in approach based upon both prior experience/lessons learned and the distinct environmental conditions of the Jezero crater landing site and season in the northern hemisphere early spring (MSL landed in the southern tropics during late northern summer). This paper is designed to document the novel aspects of the approach taken for atmospheric characterization for the Mars 2020 lander as it differed from prior missions. An understanding of the full approach to atmospheric characterization for hypersonic guided entry at Mars can be obtained by a review of the reports of CoA activities for prior missions (e.g., Vasavada et al. 2012; Chen et al. 2014), augmented by the present report.

This study begins with a review of pertinent background material and early project activities in Section 2, followed by discussion of the prelanding activities of the team in Section 3, including LSW assessments, the focused study of Jezero crater, and real-time EDL support. Sections 4 and 5 discuss postlanding activities, including reconstruction of the entry atmosphere, and a comparison of pre-EDL predictions to the reconstructed atmosphere, respectively. A summary of the high-level points is provided in Section 6.

2. Early Project Activities

2.1. CoA History

The general process of characterizing the atmosphere at Jezero crater was similar to the approach used for supporting the MSL landing at Gale crater in 2012. Following the first Mars 2020 LSW in 2014 May, the Mars 2020 CoA was assembled under the supervision of the Mars 2020 EDL team at the Jet Propulsion Laboratory to begin an initial assessment of the highest-priority landing sites as ranked from that initial workshop. The council is comprised of atmospheric specialists across many relevant disciplines, including climate modelers, instrument teams, and EDL engineers, and from a range of institutions, spanning academia, private industry, and multiple NASA centers. Council members external to NASA were selected through a competitive process overseen by the Mars 2020 project, which ensured availability of the proper expertise and tools necessary for the required evaluation tasks. A similar approach to CoA design was previously used in support of the Mars Phoenix, MSL, and InSight projects, from which many best practices were followed. Key among these practices is the blending of both available spacecraft data and numerical modeling output in order to develop the most comprehensive understanding of local atmospheric conditions, rather than relying on data or modeling alone. The primary sources of spacecraft data through much of the present effort were the Mars Climate Sounder (MCS) on board the Mars Reconnaissance Orbiter (MRO), which provided vertical profiles of atmospheric temperature and aerosol loading (both dust and water ice) from orbit, and the Mars Color Imager (MARCI) camera, also on MRO, which was used to survey the frequency and timing of potential dust storm activity that could impact the EDL season. Information from MCS was also used to evaluate atmospheric density, which will be discussed further in Section 3. Direct observations provide the backbone for the CoA work, although observations are not always available at the desired location or time of day. For example, MRO maintains a Sun-synchronous orbit with a 3 am/3 pm mean local time, providing atmospheric information over Jezero only twice daily (though periodic slewing of the MRO spacecraft allows for occasional off-nadir atmospheric observations with additional time-of-day coverage). MARCI, as a visible camera, naturally provides only once-daily images of the local daytime weather. To obtain a more thorough understanding of atmospheric behavior, then, requires the assistance of numerical models, which yield greater time-of-day coverage, high-resolution boundary layer information ($<$10 km), and winds but must be evaluated for accuracy against existing data.

A second best practice gleaned from prior missions is incorporating results from multiple numerical models into the overall atmospheric assessment. Given the stark topography and variable surface properties of the broader Syrtis Major region, which includes Jezero crater, higher spatial resolution model output is necessary to capture the influence of topography and surface conditions on the local circulation. For Mars 2020 studies, the CoA employed the Oregon State University Mars Mesoscale Model (OSU MMM) and Southwest Research Institute (SwRI) Mars Regional Atmospheric Modeling System (MRAMS) mesoscale models and considered, collectively, their output for CoA decisions. While both models rely on the NASA Ames Research Center Mars general circulation model (ARC-MGCM) to provide boundary conditions for their limited domains, the models have notable differences in architecture and heritage that can yield different results for even the same initial conditions. In the absence of sufficient in situ observations of atmospheric conditions at Mars, it is not possible to assess which model provides a more "correct" interpretation of the local atmosphere at any given time; hence, the CoA considers both models as providing equally reliable atmospheric conditions, bootstrapping upon their extensive heritage and prior validation efforts (e.g., Rafkin et al. 2001; Tyler et al. 2002, 2008; Tyler & Barnes 2013; Pla-García et al. 2016; Rafkin & Michaels 2019). Together, the two models provide a broader range of potential atmospheric conditions than either model alone. The strengths and weaknesses of the two models have been documented elsewhere (Tyler et al. 2002; Tyler & Barnes 2014; Rafkin & Michaels 2019), so this study only touches upon the new aspects of these models as they were used for Mars 2020.

To tie together the observational and modeling data, the CoA also incorporated the results of Mars data assimilation modeling efforts using the UK GCM data assimilation tool (Lewis et al. 2007; Holmes et al. 2020), itself using data from a range of spacecraft observations. Additionally, radio occultation (RO) data of surface pressure (Hinson et al. 1999, 2019) are used to ensure a globally optimized annual pressure cycle. From these results, the individual mesoscale models can be tuned to better reflect local conditions around Jezero. A similar approach was taken for prior mission studies by the CoA.

2.2. Landing Site Selection

An assessment of the landing safety of each site was conducted prior to each of the final three LSWs, which included an evaluation of the atmospheric conditions at each site and their anticipated effect on EDL performance. In advance of LSW 2 in 2015 August, the CoA completed GCM and mesoscale model simulations of multiple sites and integrated the mesoscale model output into EDL performance simulations. This enabled the CoA to evaluate eight of the top

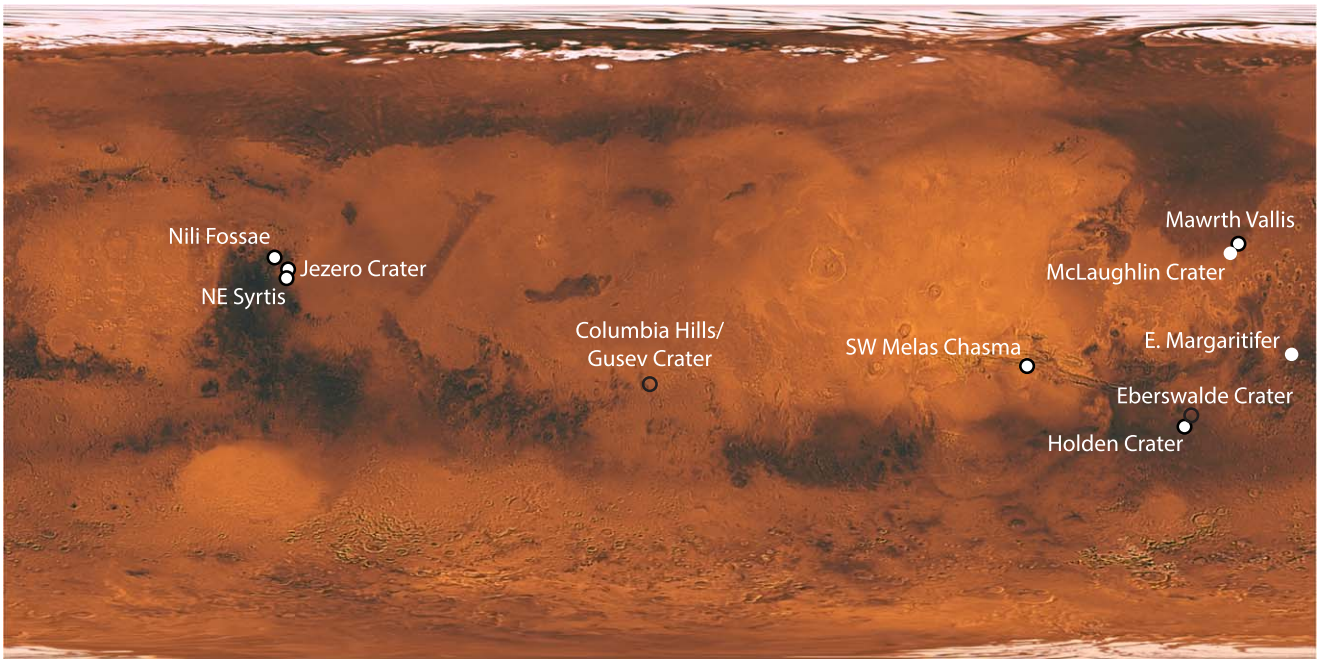

Figure 1. Map of candidate sites for Mars 2020 landing. White spots indicate sites evaluated by the CoA prior to LSW 2. Sites with black rings were the final eight sites under consideration after LSW 2, all of which were ultimately evaluated by the CoA. Jezero crater (18.°38N, 77.°58E) was the chosen landing site.

nine sites at the time (McLaughlin crater, E Margaritifer, Holden crater, Jezero crater, Mawrth Vallis, NE Syrtis, Nili Fossae, SW Melas Chasma, and the Nili Fossae carbonate region; Figure 1) and provide a preliminary atmospheric assessment for each site. Atmospheric evaluation of the Nili Fossae carbonate region was suspended pending resolution of a separate engineering assessment of its terrain, and the site was ultimately removed from consideration. At each landing site, the CoA evaluated whether there was a general agreement between the numerical models (especially for wind magnitude and direction) and whether EDL performance was acceptable for the given mesoscale model results. For LSW 2, the CoA provided "green" status (indicating acceptable atmospheric conditions) for all eight sites and noted that the identified issues (such as model variations in wind feature location/strength) were minor and not expected to significantly impact the overall EDL performance.

Between LSW 2 and LSW 3, the CoA continued their evaluation of the landing site candidates. First, the CoA performed model simulations of two new candidate landing sites that were introduced: Eberswalde crater and Columbia Hills/Gusev crater. Second, dust storm statistics were generated for the top eight sites to gauge the frequency and size of dust storm activity during the northern spring EDL season, around $L_s = 5°$ (Cantor et al. 2019). Even though it was found that the likelihood of a dust event was very low, "dusty" mesoscale simulations were subsequently generated for the three Syrtis region sites: NE Syrtis, Jezero crater, and Nili Fossae. Furthermore, the NE Syrtis dust storm mesoscale data were run through EDL performance simulations showing that the EDL system could handle atmospheric wind and density perturbations introduced by local-to-regional-scale dust storms (Section 3.5.2). For LSW 3, the CoA again reported acceptable EDL performance at the top eight sites using nominal (i.e., clear sky) atmospheres but noted that further investigation would be necessary for SW Melas, Mawrth, and Columbia Hills if they were still considered after LSW 3.

Between LSW 3 (2017 February) and LSW 4 (2019 October), the CoA conducted two independent peer reviews (2017 April and 2018 April) of its progress with a board consisting of atmospheric scientists and engineers who were unaffiliated with the Mars 2020 project but had relevant experience and familiarity with Mars EDL from prior missions. The main objective of these independent peer reviews was to evaluate the process undertaken by the Mars 2020 CoA and verify that the full range of plausible atmospheric conditions for EDL had been identified and bounded conservatively. Recommendations and findings from the review board were implemented by the CoA going forward. For LSW 4, the CoA reported nominal atmospheric conditions and acceptable EDL performance at the remaining top four sites (Columbia Hills, Jezero crater, NE Syrtis, and the newly minted "Midway" site, located between NE Syrtis and Jezero) but noted greater differences in zonal wind profiles between the mesoscale models at the Columbia Hills site, which would have led to slightly greater uncertainty in the atmospheric state going forward.

3. Prelanding Activities

3.1. Mesoscale Modeling

Drawing on experience from CoA activities for MSL (Vasavada et al. 2012), mesoscale simulations of the Syrtis Major/Jezero crater region were developed for both nominal and off-nominal conditions in order to provide a broad range of potential atmospheric conditions to the Mars 2020 EDL team. Nominal conditions entailed the best prediction of the atmosphere at landing, including consideration of seasonal dust loading. Off-nominal conditions included scenarios of plausible (though unlikely) dust activity, including regional and local dust storms that could impact atmospheric heating and thus density. A summary of these individual scenarios is provided below for each of the two mesoscale models used by the CoA.

3.1.1. OSU MMM

The OSU MMM, as first described by Tyler et al. (2002), is the first of two models used to characterize the Martian atmosphere for Mars 2020 EDL. The model settings unique to the Mars 2020 EDL activity are described below. Initial and boundary conditions (hourly) for the OSU MMM are provided by a version of the ARC-MGCM developed and maintained at OSU. The ARC-MGCM is run in a "seasonal mode" for a total of 60 sols, where the final 10 sols are centered in solar longitude on the season of Mars 2020 EDL ($L_s = 5°$). The ARC-MGCM is configured on a rectangular $5° \times 6°$ Arakawa C-grid and uses a sigma pressure vertical coordinate (where the model top is at 1×10^{-4} mb). The seasonal cap boundaries in the ARC-MGCM are prescribed as a function of L_s, and the initial atmospheric mass is tuned so as to provide very good agreement with the surface pressure evolution as observed by the Viking 1 lander. This results in the mean diurnal surface pressure simulated in the OSU MMM being climatologically accurate for the Mars 2020 EDL season, meaning that no tuning adjustment of the model results was required before incorporating model data into the engineering simulations.

The OSU MMM and ARC-MGCM share the same correlated-k atmospheric radiation scheme (see Haberle et al. 2019). This scheme takes advantage of an improved dust prescription that was developed during the initial stages of the Mars 2020 work. The two key parameters in the new dust prescription are (1) the surface dust opacity (TAU) and (2) the Conrath-Nu parameter (CNp). In this new prescription, both quantities are defined in 2D (lat x lon), not as zonal means, as done for MSL. Additionally, both parameters are now derived directly from observations. The 2D TAU value at the L_s of EDL is constructed via an analysis of Thermal Emission Spectrometer (TES) column dust opacity data at the surface (Michael Smith, personal communication). For the vertical distribution of dust, the 2D CNp is constructed via an analysis of MCS dust density-scaled opacity (Heavens et al. 2011a, 2011b) over a narrow range of L_s spanning the date of EDL and for a number of Mars years (MYs). Having the vertical distribution of the MCS dust mixing ratio with pressure allows the construction of a pressure "top" for the atmospheric dust (the pressure where the mixing ratio decreases rapidly in the vertical to some very small value). With that value (P_{top}) determined at all locations, the pressure difference to the surface ($P_{sfc} - P_{top}$) is converted to a number of scale heights (H) that describes the depth of atmospheric dust. From that quantity, the local value of CNp is given by $\mathrm{CNp} = \exp(-H)$. After filling in some small data gaps and with minimal smoothing, the constructed values of H and TAU, as used in the dust scheme for this modeling, were finalized and are shown in Figure 2.

In comparisons between ARC-MGCM runs that used either the 2D parameters or the older approach with zonal means, no difference is observed between the zonal mean temperature fields using either approach, which served as a basic confirmation of the efficacy of the new method. However, for specific locations in the GCM, the differences between the two approaches did become significant. This new dust prescription aligns better with the observed seasonal dust distribution, and it may indeed be the case that the reasonably good agreement seen aloft between OSU MMM temperature profiles and actual MCS temperature profiles in the Jezero crater region (see Section 3.6) is a consequence of this more realistic dust scheme.

For this work, the OSU MMM was configured to run with a mother domain and three nests (higher-resolution subdomains). The mother domain (grid 1), which interacts with the hourly ARC-MGCM boundary conditions, is polar stereographic and centered on the north pole of Mars because of the northern hemisphere location of Jezero crater. Nominal grid spacing is 108 km (this resolution is "true" at 20°N and stretched elsewhere), and the mother domain has a size of 150×150 grid points. The vertical coordinate in the OSU MMM is sigma pressure (identical to that of the ARC-MGCM), with 55 layers in the vertical that are configured to provide very good vertical resolution through the lowest ~40 km of the atmosphere. The lowest model layer is ~5 m above the surface, with 27 layers falling within the lowest 10 km. The model top of the OSU MMM is 1×10^{-4} mb. Each level of nesting in the OSU MMM increases the spatial resolution in the model by a factor of 3, which results in a nominal spatial resolution for the highest-resolution nest (grid 4) of 4 km. The OSU MMM uses surface properties derived from TES and MOLA data. Surface albedo and thermal inertia are obtained from Christensen et al. (2001) and Putzig & Mellon (2007), respectively. Surface topography is derived from MOLA measurements, as discussed in Smith et al. (2003). The model also incorporates the medium-range forecast model boundary layer scheme (Hong & Pan 1996) to address vertical diffusion of mass and momentum in the lower atmosphere and a five-layer surface–subsurface model that allows thermal exchange between the subsurface and the atmosphere.

In general, two key design criteria must be taken into account when developing mesoscale models to support spacecraft EDL: (1) the location, resolution, and spatial extent of any nested domains are central to realistic simulations of mesoscale circulations; and (2) the spatial coverage of the planet surface, as related to the surface transect of the EDL flight path, is important so that high-resolution results for engineering simulations are available along the EDL trajectory (this point is reiterated in Section 3.5.1). Regarding the highest-resolution nests in the OSU MMM, satisfying the second criterion can be difficult. For Jezero crater, the topography of nests 2 and 3 (nominally at resolutions of 12 and 4 km) is shown in Figure 3. During EDL, spacecraft entry would be from the WNW, and output from both nests would be needed to supply data to the engineering simulations. The 12 km nest (left panel in Figure 3) was also designed in consideration of the strong regional circulations influenced by the sharp topography around Jezero crater that are expected and simulated in mesoscale models at the season of Mars 2020 EDL.

The complex topography in and around Jezero crater and the Syrtis Major region generates strong regional mesoscale circulations, and the depth of the afternoon convective boundary layer (CBL) serves as an important diagnostic that is regularly used to guide investigations into the modeled atmosphere. Given the rapid decrease in vertical mixing at the top of the CBL, it is at the top of the CBL where large changes in wind speed and direction are certain to occur. For Mars 2020 EDL, spatial variation of the CBL top occurs right along the spacecraft trajectory. This spatial variation is depicted in Figure 4, where the CBL depth is shown for the 12 km nest (nest 2). For the CBL depth in Figure 4, a total of 10 sols of semihourly model output were used to construct the CBL depth during the local solar time window of 14:30–15:30. In Figure 4, it can be seen that the CBL is very shallow over Jezero crater—between ~2 and 4 km, which means the spacecraft would

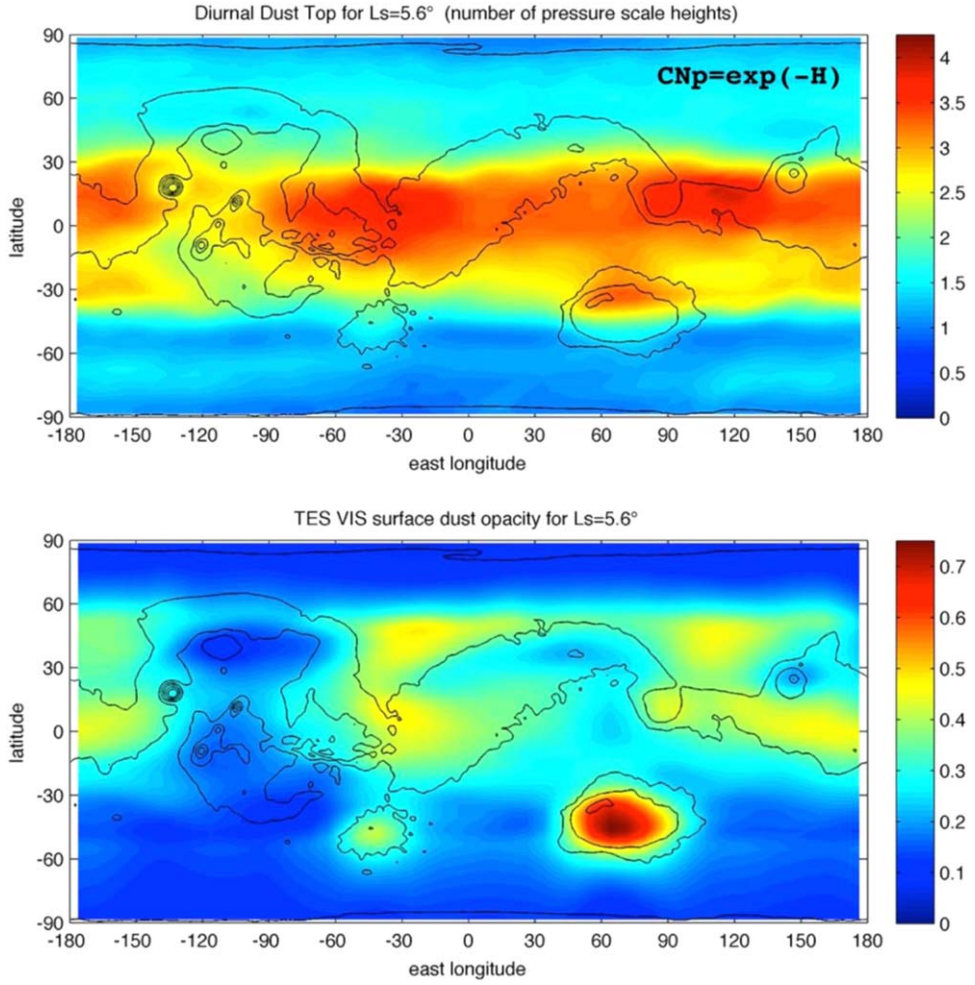

Figure 2. The 2D parameters of the dust scheme as used in the ARC-MGCM and OSU MMM are shown. These data are constructed using the pressure level vertical coordinate of the MCS dust density-scaled opacity data (top) and the TAU from TES (bottom). The TES IR opacity is scaled by 2.25 to approximate 0.67 μm TES VIS opacity. For spatial orientation, topography is indicated with black contour lines.

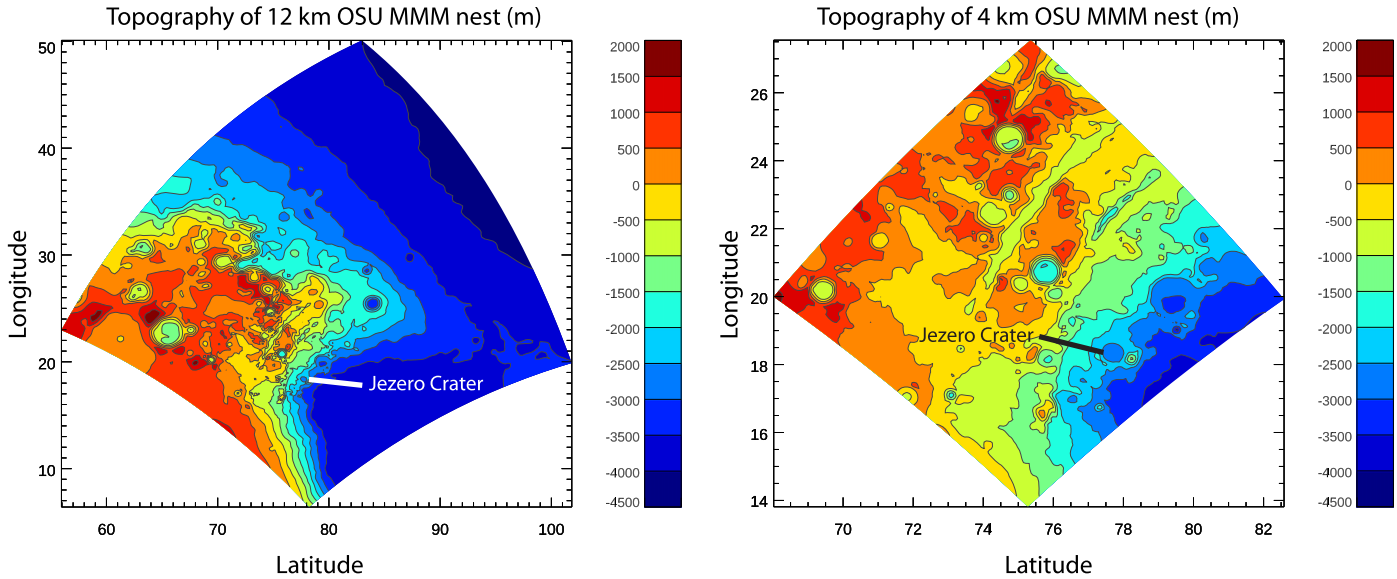

Figure 3. Topography (in m) of grid 3 (left) and grid 4 (right) in the OSU MMM. Each grid has 145 × 145 points. The location of the Mars 2020 landing site in Jezero crater is indicated.

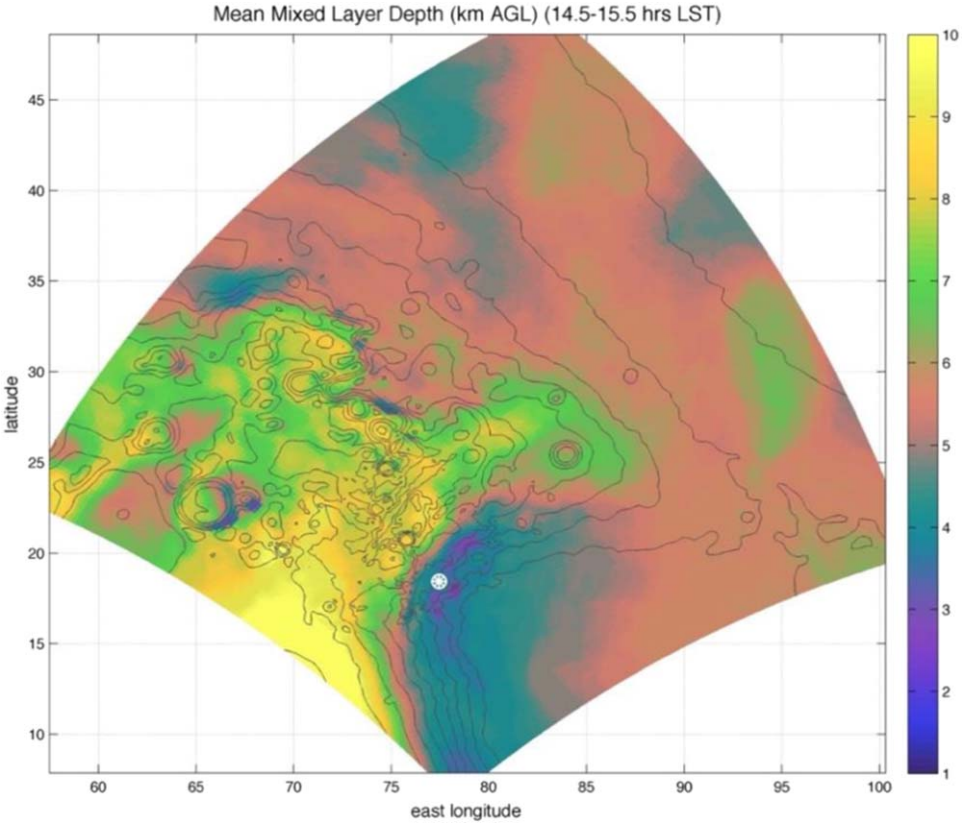

Figure 4. Afternoon depth of the CBL, as simulated with the OSU MMM, for Mars 2020 EDL into Jezero crater. The CBL depth (in km) is shown with color for nest 2, and thin black contour lines provide topographical reference. The location of the Jezero crater landing site is marked with a circled white asterisk.

be in the "free" atmosphere at this location while under parachute until very near the ground. Earlier along the EDL trajectory, though, the CBL can be quite deep (~10 km). The consequence of this change in CBL depth is that there is a great deal of variation observed in the simulated winds along the nominal EDL trajectory, transitioning from below to above the top of the CBL. This reality, and the strong regional mesoscale circulation that generates it, does make EDL at this season into Jezero crater somewhat challenging. The terrain relative navigation (TRN) developed for Mars 2020 EDL (Johnson et al. 2017, 2022) is therefore an important technological development that is quite useful for more precise landings under the influence of such challenging atmospheric conditions.

The atmospheric dynamics that cause such expected variation in the depth of the CBL are described in Tyler & Barnes (2015). Additionally, Hinson et al. (2019) provided an interesting comparison study between RO temperature observations and model results from a different OSU MMM simulation that was performed for a slightly later seasonal date ($L_s = 40°$). The RO observations pertinent to Mars 2020 are revisited in Section 3.4. The circulations that produce such dramatic variation in the afternoon CBL depth on Mars appear to be quite prolific and also appear across a very wide range of scales.

3.1.2. SwRI MRAMS

The MRAMS (Rafkin et al. 2001; Rafkin & Michaels 2019) is the second of the models used to characterize the Martian atmosphere for Mars 2020 EDL. This same model was used successfully for atmospheric characterization at the Mars Exploration Rover (Rafkin & Michaels 2003), Phoenix lander (Michaels & Rafkin 2008), Beagle 2 lander (Rafkin et al. 2004), ExoMars Demonstration lander (Bertrand et al. 2013), InSight lander (Maddock et al. 2020), and MSL (Vasavada et al. 2012; Chen et al. 2014) landing sites. Confidence in the model results is bolstered by a favorable comparison with the in situ meteorological data returned from the Rover Environmental Monitoring Station on the Curiosity rover (Pla-García et al. 2016).

The MRAMS is configured with five nested grids. It uses a generalized oblique polar stereographic projection with a user-specified pole point and grid locations (Rafkin et al. 2001). Grid 1 has a horizontal spacing of 240 km. Each nested grid has spacing three times smaller than its parent, which results in ~2.96 km spacing on the highest-resolution grid (grids 3 and 4 are shown in Figure 5). A mother domain centered close to the landing region is preferred over a domain centered over a pole in order to avoid potentially serious physical and numerical issues of the type discussed in Rafkin & Michaels (2019). The chosen grid configurations take into account potential numerical issues and computational efficiencies inherent to grid-point modeling, the desire to capture flows from potentially influential topographic features (e.g., Hellas basin), and the desire to avoid intersecting extreme topographic features with a grid boundary as much as practical. Since the Jezero crater landing site is along the rim of Isidis basin, the intersection of that crater rim by some grid boundaries is unavoidable. Tests of different grid configurations were conducted for multiple proposed landing sites prior to the final downselect to Jezero crater. The result of the test cases

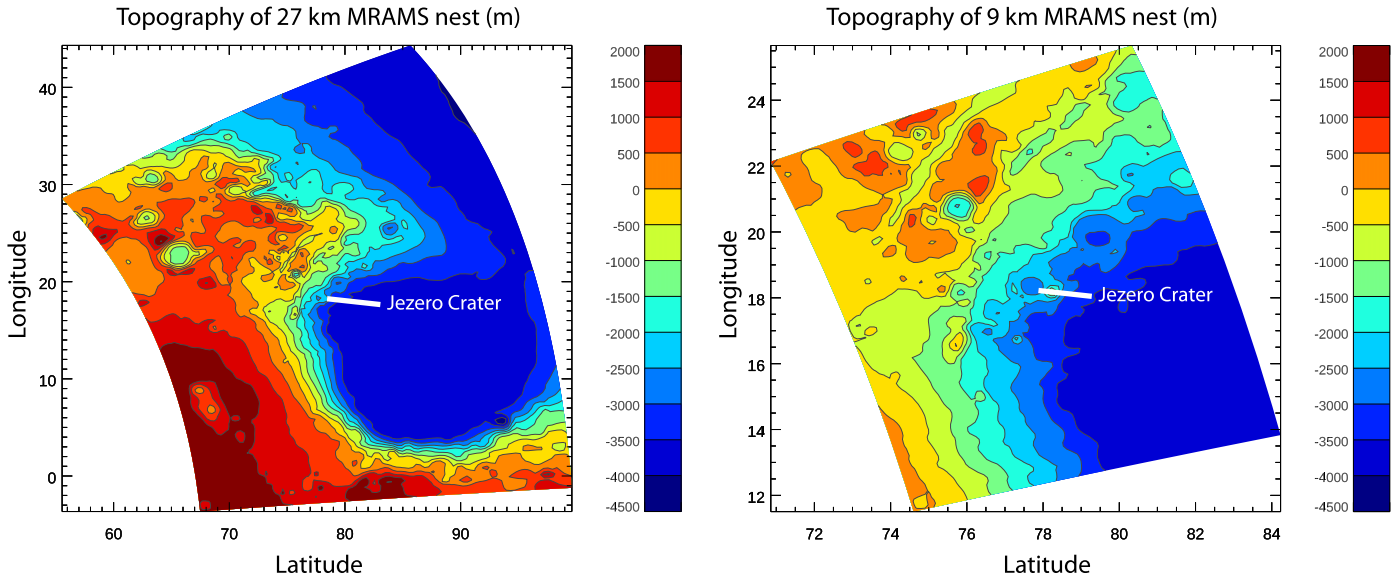

Figure 5. Topography (in m) of grid 3 (left) and grid 4 (right) in MRAMS. The model is configured with five nested grids. The grid spacing on the mother domain grid is 240 km at the map projection point of 10°N, 143°E. The location of the Mars 2020 landing site in Jezero crater is indicated.

indicates that the grid with the least map projection distortion at the landing site provides superior performance, all other things being equal.

The terrain-influenced vertical grid has the first atmospheric level at ∼14 m above the ground. The 50 vertical levels in MRAMS gradually stretch from a spacing of ∼30 m to a maximum of 2500 m at the model top of ∼50 km. The top five layers serve as damping layers with a gradually increasing Rayleigh friction timescale corresponding to a timescale of 30 s in the uppermost model layer. The time step on the mother domain is 10 s and decreases to 0.625 s on grid 5. The time step is driven primarily by stability conditions related to vertical motion. As with the OSU MMM model, thermal inertia and albedo values are specified based on those derived from the gridded Mars Global Surveyor TES data with 1/8th degree binning (Putzig & Mellon 2007; Christensen et al. 2001). Model topography is based on the MOLA 1/128th degree digital elevation product (Smith et al. 2003). Initial and boundary conditions are provided by the ARC-MGCM, though with an implementation that differs from that used by the OSU MMM. Boundary conditions are updated every 1.5 Mars hr. For the Mars 2020 assessment, all model domains are integrated concurrently for 5 sols, and the first sol of data is discarded so as to remove model spin-up transients. Model fields of temperature, pressure, 3D wind components, and subgrid-scale turbulent kinetic energy are output at a frequency of 1/12th of a Mars hour (i.e., every 5 Mars minutes).

The physical processes active in MRAMS include its standard suite: two-stream correlated-*k* radiative transfer, a Monin–Obukhov surface layer, a level 2.5 prognostic turbulent kinetic energy subgrid diffusion closure, and a surface–subsurface model coupled to the atmosphere allowing thermal exchange between the subsurface and atmosphere. All of these processes are described in Rafkin et al. (2001) and Rafkin & Michaels (2019). Atmospheric dust loading is typically fixed to seasonal TES-based values with a seasonally and latitudinally dependent Conrath-nu vertical profile. The latitude-only dependence of the CNp is different from the lat/lon dependence of the same in the OSU MMM and discussed in Section 3.1.1.

A fully interactive dust-lifting parameterization was activated in a limited number of simulations to assess the potential impact of local-to-regional dust storms. In these cases, the dust-lifting threshold and dust mass flux efficiency were iteratively tuned to produce an evolving local storm near the landing site (Rafkin et al. 2017). Comparison of the active dust-lifting simulations with the static, seasonal dust distribution simulations pinpointed the atmospheric perturbations resulting from local and regional dust disturbances near the landing site. An advantage of the interactive dust-lifting methodology is that the atmosphere structure, dust, and dust lifting evolve in a fully and physically consistent way. In contrast, imposing dust forcing from a user-specified dust disturbance necessarily means that the initial wind and thermal structure are not consistent with atmospheric dust loading, and the tight coupling between dust lifting, atmospheric dust loading, dynamics, and thermodynamics may not be accurately represented. A disadvantage of the interactive method is that it is difficult to precisely control the location, timing, and movement of the resulting dust disturbances. For example, no disturbances formed directly over the landing site. The active dust disturbances were typically associated with local anabatic and katabatic flows (i.e., slope winds up and down the walls of the Isidis basin, respectively), and the radiative forcing from curtains of dust lifted along the upslope/downslope fronts resulted in a substantial modification of the thermal and kinematic wind structure compared to the static simulation.

In MRAMS, atmospheric density is diagnosed from predictions of pressure and temperature via the ideal gas law. Since MRAMS is not a global model, it inherits the mass distribution, and any errors, from the ARC-MGCM. The mapping of the coarse ARC-MGCM fields to the higher-resolution MRAMS grid can further modulate the mass field, for which pressure serves as a proxy. Finally, the compressible, nonhydrostatic dynamical core of MRAMS, coupled with the radiative forcing, can also generate a bias in pressure compared to the ARC-MGCM. In the absence of an accurate reference

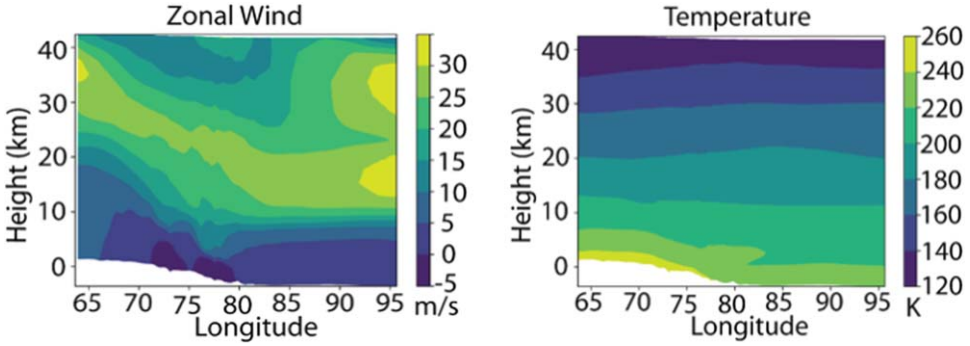

Figure 6. West–east vertical cross sections of zonal wind and temperature along 18.°38N on MRAMS grid 3 for simulation sol 4 at 15:53 LMST. White shading is below ground.

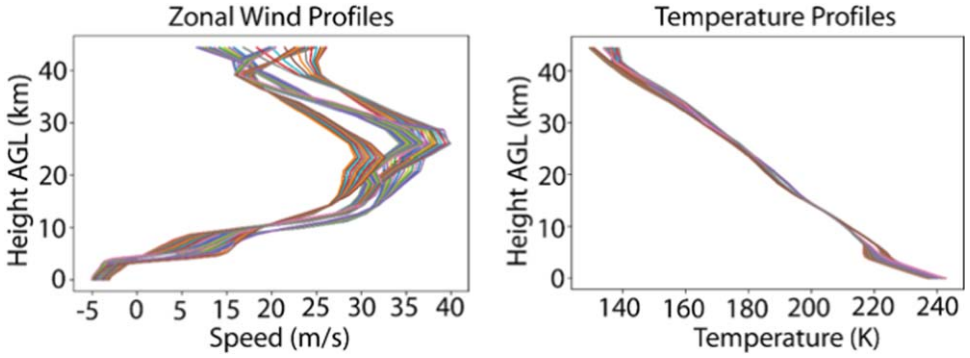

Figure 7. Vertical profiles of zonal wind and temperature on MRAMS grid 5 for sols 2, 3, and 4. Each cluster of 12 lines corresponds to 1 hr of data for 1 sol centered on the landing time of 15:53 LMST.

pressure, only the variation of MRAMS pressure, rather than absolute pressure (or absolute density), is generally utilized, as discussed in Rafkin & Michaels (2019). For the present work, a reference pressure was obtained from the OpenMARS reanalysis database (Holmes et al. 2020) discussed in Section 3.3. Given a reference pressure from this reanalysis, the MRAMS pressure field was rescaled by a factor of 1.039, as described in Rafkin & Michaels (2019). The rescaling of the pressure does not affect the hydrostatic balance and has a negligible impact on temperature or wind fields. This rescaled pressure is then used to determine atmospheric density.

Sample west–east (i.e., zonal) vertical cross sections of zonal winds and temperature from grid 3 near the time of landing (15:15 LTST/15:53 LMST) are shown in Figure 6. Vertical profiles of wind and temperature from the model point closest to the center of the landing ellipse on grid 5 are shown in Figure 7. Temperature variations are the primary cause of the density variations that are of interest for EDL. A westerly jet is present at an altitude of ∼35 km at the western edge of grid 3 to the west of Isidis basin. The jet descends as the topography drops toward Isidis. East of the landing site, a double jet structure emerges.

At the landing site (Figure 7), the height of the jet varies between 25 and 30 km from sol to sol. Surface temperatures are warmest on the elevated topography west of Isidis, but the temperatures aloft are slightly colder compared to temperatures further east. Along the edge of Isidis, very near the longitude of the landing site, a weak temperature inversion is found at ∼5 km altitude. This structure shows up clearly in the temperature profiles of Figure 7. The typical afternoon adiabatic layer (i.e., the near-surface region having a constant potential temperature) is present below the inversion, which roughly indicates the top of the CBL.

3.2. Mesoscale Model Validation

As part of the CoA preparations, the results from the mesoscale models and the global MGCM runs used for their initial and boundary conditions are compared to relevant MCS observations, with the goal of validating the model performance. While general model validation has been extensively performed for all of the models, as discussed in Section 2, this particular validation effort is focused on the specific season and landing location for Mars 2020, including consideration of local and regional topography, as well as the choice of mesoscale grid and aerosol representation. These comparisons were performed multiple times over the development cycle of the mesoscale models and the downselection of the landing sites.

The MCS profiles are available at the Mars 2020 landing season in six MYs (MY 29 and MY 31–35; some of the earlier validation efforts used fewer MYs). In all MYs, the standard MCS profiles are available with an LTST of ∼14:10 (ranging from 14:05 to 14:18, or ∼14:43–14:56 LMST). Profiles at a later local time (∼15:50 LTST/16:28 LMST) are also available in MY 31–34 and were used in some of the comparisons to bracket the expected landing local time of 15:15 LTST/15:53 LMST.

Two types of comparisons between model and data are performed. The first type of comparison is of the models to regional/global observations. The second type is a comparison of the models to specific landing site locations. For the regional/global comparisons, typically, MCS zonal mean cross sections of temperature are calculated. Cross sections of dust and water-ice clouds are also examined but are not really

comparable to the models (since the mesoscale models do not have water-ice clouds, and, in most cases, the model dust fields are at least partly prescribed). In some cases, longitudinally restricted (30° longitude) bins are used to understand the zonal structure of the atmosphere and its impact on different landing sites. For the zonal average, a standard seasonal window between $L_s = 2°$ and 9° is used. At this season, the interannual variability is quite low, with a variance of <2 K throughout most of the atmosphere.

Figure 8 shows a comparison between zonal mean temperature cross sections for MY 32 from the ARC-MGCM as used by MRAMS (top) and OSU MMM (middle) and MCS data (bottom) for the same MY and season. Here the ARC-MGCM implementation for the OSU MMM has been tuned by adjustment of the CNp (Section 3.1.1) to provide the best match to the MCS data. No such tuning was performed for the MRAMS implementation. Because of the low interannual variability, the other years are essentially indistinguishable at this season. The cross sections from both models show the classic equinoctial circulation pattern and resulting temperature structure for Mars for both nighttime (02:10 LTST; left column) and daytime (14:10 LTST; right column). As expected, there are two overturning (Hadley) cells, rising in the equator and descending over each pole, encompassing a pair of active, cold (although not at the CO_2 condensation temperature) polar vortices. The descending branches produce strong adiabatic warming above both vortices that slants from the pole to the midlatitudes. Near-surface warming is essentially symmetric about the equator (since the subsolar point at this season is over the equator). There is a strong day/night temperature difference due to the diurnal thermal tide that is symmetric in both hemispheres.

Comparing the ARC-MGCM output from the two models to the MCS data shows substantial similarities at this season. The overall two-branch structure is correctly captured. In addition, the MGCMs show the difference in temperatures between the north and south descending branches, as well as the "flat" daytime tropical temperatures at ∼0.1 mb (right column) compared to the more "dome-shaped" temperatures at night (left column). Both MGCM instances are somewhat colder at altitudes above ∼0.05 mb at most latitudes, although they have stronger antinode signatures of the diurnal tide, and a few of the warm phases are warmer than seen in the data, especially for the MRAMS implementation. The differences are likely due to the limitations of the aerosols in the MGCMs, especially the lack of radiatively active clouds (which were deliberately turned off to align the mesoscale model physics).

For the second type of comparison, targeting specific landing sites, a bin in latitude, longitude, and L_s is used to select the relevant available profiles around each target location and season. The standard bin used is ±15° in latitude and longitude and ±3°.5 in L_s. Depending on the specific investigation, the MCS-retrieved profiles might be either partitioned by MY and/or local time or combined together. Figure 9 shows all MCS profiles (1088 total) taken at LT ∼14:10 over all available MYs near the Jezero crater landing site. The retrieved temperatures show a fairly typical tropical equinoctial structure. Near the surface, there is a broad spread of temperatures driven by the local elevation within the 15° bin and other local conditions (surface albedo, etc.). The general trend is one of temperatures being warmest in the southern highlands to the west of Jezero and coldest in the Isidis basin to the east. This matches what is seen in the MRAMS mesoscale results (Figure 6). There is an overall oscillating wave pattern in the vertical (likely tidally driven) superimposed on the lapse rate starting at around 1 mb. At high altitudes, above 0.01 mb, the MCS measurement uncertainty increases; however, relatively large-amplitude waves also contribute to the variability. At this season and region, there is very little interannual variability, as shown by the lack of separate profile families for each MY in Figure 9. Model comparisons to these MCS data will be revisited in Section 3.5.3.

3.3. Surface Pressure Modeling

Spacecraft engineers are most concerned with atmospheric density and wind shears to ensure safe EDL. As was found to be the case for Curiosity EDL (Vasavada et al. 2012), it is essential to predict surface pressure in order to constrain density–altitude profiles from either models that work in a vertical, pressure-based coordinate or using remote-sounding observations from which temperature is usually retrieved as a function of pressure (e.g., Conrath et al. 2000; Smith 2004; Kleinböhl et al. 2009, 2017). The surface pressure on Mars is, however, highly variable. It varies with the time of year as a result of condensation and sublimation of carbon dioxide at the polar caps (Hess et al. 1980) and seasonal changes in the mass distribution of the atmosphere (Hourdin et al. 1995). Surface pressure also varies from day to day as a result of large-scale weather systems (e.g., Read & Lewis 2004; Barnes et al. 2017) and diurnally owing to the relatively large magnitude of the Martian thermal tides (Wilson & Hamilton 1996). Thermal tides include both Sun-synchronous and asynchronous modes, which vary strongly in amplitude with atmospheric dust loading (Lewis & Barker 2005; Guzewich et al. 2016). Surface pressure can also fluctuate on very short timescales because of convection in the planetary boundary layer (Read et al. 2017), although these fluctuations are generally small in amplitude compared to the previous sources of variability, except for the most powerful convective vortices, which can exhibit an amplitude of about 10 Pa (Spiga et al. 2010a, 2010b; Fenton et al. 2016).

Seasonal, day-to-day, and diurnal variations in surface pressure can be represented in a GCM (see, e.g., Haberle et al. 1993; Forget et al. 1999; Richardson et al. 2007), even without very high horizontal resolution. In regions with large topographic contrasts, in particular, the capture of more detailed behavior does require the use of mesoscale models like the OSU MMM or MRAMS, though they will not necessarily be able to represent the large- to global-scale wave dynamics; for example, thermal tidal modes may be forced by variations in suspended dust over planetary scales (Wilson & Hamilton 1996). Global-scale tidal modes often account for the largest proportion of the diurnal variability in surface pressure. The procedure used here to predict surface pressure largely follows that described by Vasavada et al. (2012), with the major difference being access to a much longer reanalysis record that includes nine MYs, during five of which thermal and dust opacity data from MCS were available to help in the analysis.

Surface pressure was extracted from a nine-MY reanalysis record, a publicly available version of which is known as the OpenMARS database (Holmes et al. 2020). At the time that the reanalysis effort commenced in 2016, observations in the period MY 24–32 (1998 July–2015 June) were available for

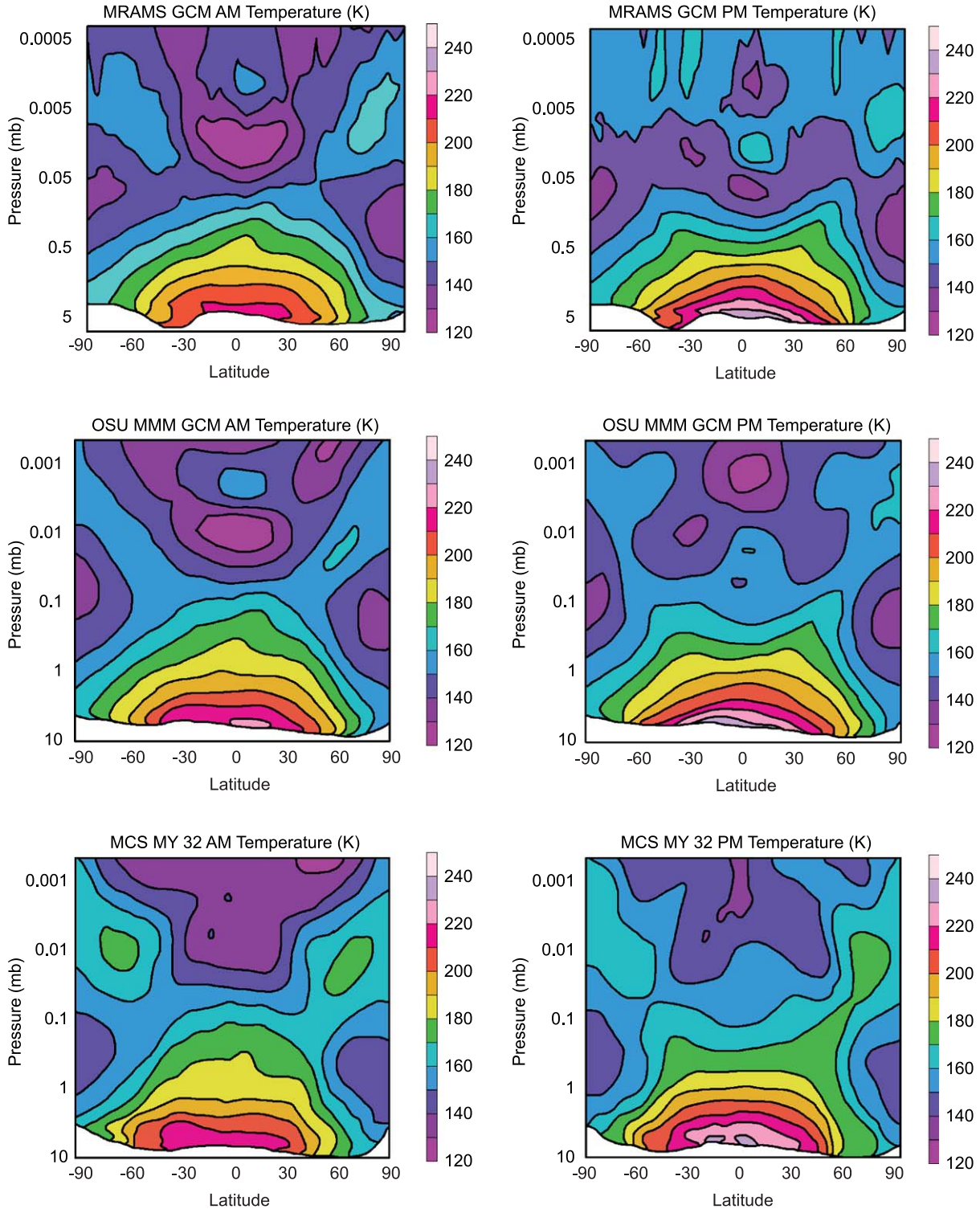

Figure 8. Zonal mean temperature cross section at the Mars 2020 landing season in MY 32 for the MRAMS GCM (top), OSU MMM GCM (middle), and MCS (bottom). The left column shows nighttime observations (02:10 LTST), and the right column shows daytime observations (14:10 LTST).

assimilation, so the work was based on these years; subsequent years were analyzed later as retrievals became available but did not significantly alter the predictions for EDL. A true weather forecast was not attempted due to the complexity of the operations required to implement real-time data assimilation. The CoA predictions were, therefore, based on the average climatology and a selection of years in the reanalysis period. This was reasonable, since the day-to-day weather variability was generally small at this site and time of year compared to seasonal and diurnal cycles, but its magnitude could be estimated from the nine MYs in the record and contribute to the uncertainty in estimates provided to the EDL engineers.

The atmospheric reanalysis was formed by combining an evolving atmospheric forecast, made using the Open University version of the LMD-UK GCM (Forget et al. 1999), with observations where and when they became available. This

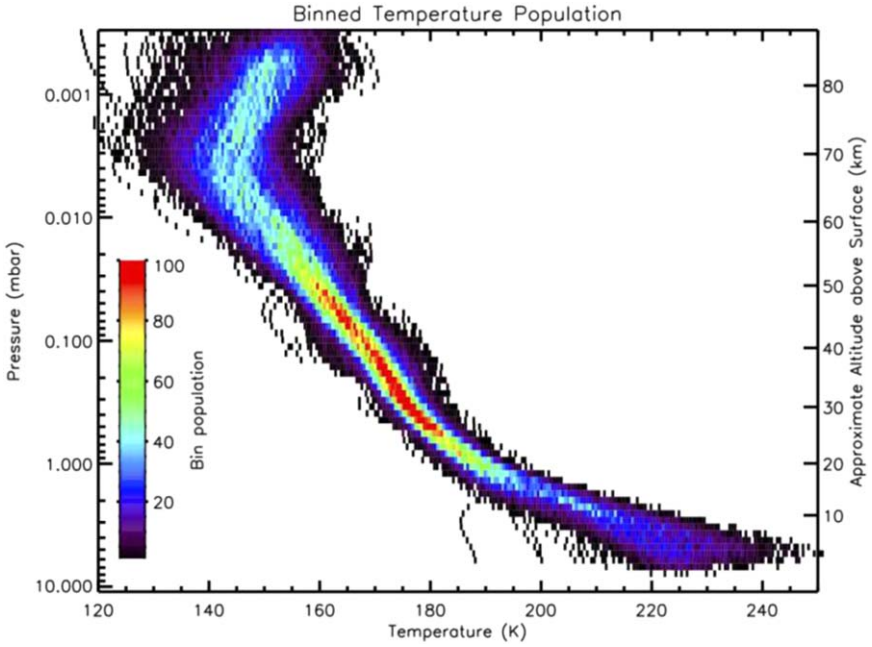

Figure 9. The 1088 historical MCS temperature profiles at the Jezero crater landing site for all six available MYs, with observations taken at an LTST of ∼14:10. The colors are a temperature histogram at each MCS pressure level, showing the number of profiles in each 0.5 K temperature bin.

process is known as data assimilation, and the scheme used is described for Mars by Lewis et al. (2007). More technical details of the assimilation used to form this reanalysis are given by Holmes et al. (2020). The main sources of data employed in this period are nadir-sounded temperature profiles and total dust opacity (Conrath et al. 2000; Smith et al. 2000; Smith 2004) from TES from $L_s = 104°$ in MY 24 to $L_s = 81°$ in MY 27 and MCS limb temperature and dust opacity profiles (Kleinböhl et al. 2009) from $L_s = 111°$ in MY 28 to the end of the reanalysis period. Within each of these main periods are several shorter interruptions to the coverage (e.g., as a result of solar conjunctions), and these were taken into account when selecting data for assimilation. A single, continuous reanalysis was run over the full period using interpolated total dust opacities from Montabone et al. (2015) to constrain the MGCM whenever TES or MCS observations were not available.

The MGCM used in the reanalysis is also as described in Holmes et al. (2020), with a spectral dynamical core and a semi-Lagrangian tracer advection scheme (Newman et al. 2002) coupled to physical parameterizations developed in a multiteam collaboration (Forget et al. 1999), including an updated planetary boundary layer scheme (Colaïtis et al. 2013), a photochemical module (Lefèvre 2004), and a water microphysics scheme (Navarro et al. 2014). The atmospheric model variables (surface pressure, wind, and air temperature) are recorded on a regular $5° \times 5°$ longitude–latitude grid, at each point of which a series of 1D, vertical submodels are run to describe the parameterizations. These include subsurface heat transport, surface properties and ice, radiative transfer, dust distribution, and water microphysics, which are also recorded and, in turn, impact back upon the atmospheric variables. The MGCM is initially run with 35 vertical levels extending to an altitude of around 105 km for the whole period, with later years subsequently reanalyzed with 70 vertical levels covering the same range.

Model surface pressures were bilinearly interpolated to the landing site, initially for all sites under consideration at the LSWs and, later, specifically for Jezero crater. For Jezero, the point 18.°4386N, 77.°5031E was selected (the exact point was adjusted several times during the study). Since the model topography is determined on a discrete grid, it does not, in general, match the actual topographic height at any point on the surface. At the landing site in Jezero crater identified above, the MGCM surface is at −2003 m, compared to the surface height of −2617 m in the MOLA topographic data set (Smith et al. 2003). The resulting bias in surface pressure is removed as follows: the fixed temperature profile from the reanalysis is shifted downward to the MOLA surface such that the bottom of the reanalysis profile is made to align with the true surface height, and a pressure correction is obtained through hydrostatic integration between the MGCM and MOLA surface elevations. The 614 m change in elevation results in an increase in the predicted surface pressure of about 5.7% (40 Pa) at the time of day of EDL. This large hydrostatic correction emphasizes the value of the reanalysis in deriving the best estimate of the thermal profile.

The reanalysis does not include any surface pressure observations, which are only available at a few sites and over restricted time ranges on Mars and are insufficient to constrain the assimilation. Surface pressure is available from the Curiosity rover, but its location in Gale crater means a very much greater hydrostatic correction to the MGCM surface and corresponding uncertainties. Surface pressure observations are, instead, used to verify the procedure adopted for the prediction. First, the MGCM is tuned to best fit the Viking Lander (VL) pressure curves (Hess et al. 1980) over the course of a full annual cycle (following Hourdin et al. 1995). The reanalysis is then run with the best fit to the total available carbon dioxide mass, but the surface pressure is allowed to evolve freely in a physically consistent way with the thermal and wind fields in the MGCM. Finally, a surface pressure estimate is made at the VL 1 site using a hydrostatic correction as above and compared with the actual VL 1 curve, both smoothed on 30 sol timescales to remove weather fluctuations, and comparing the cycles

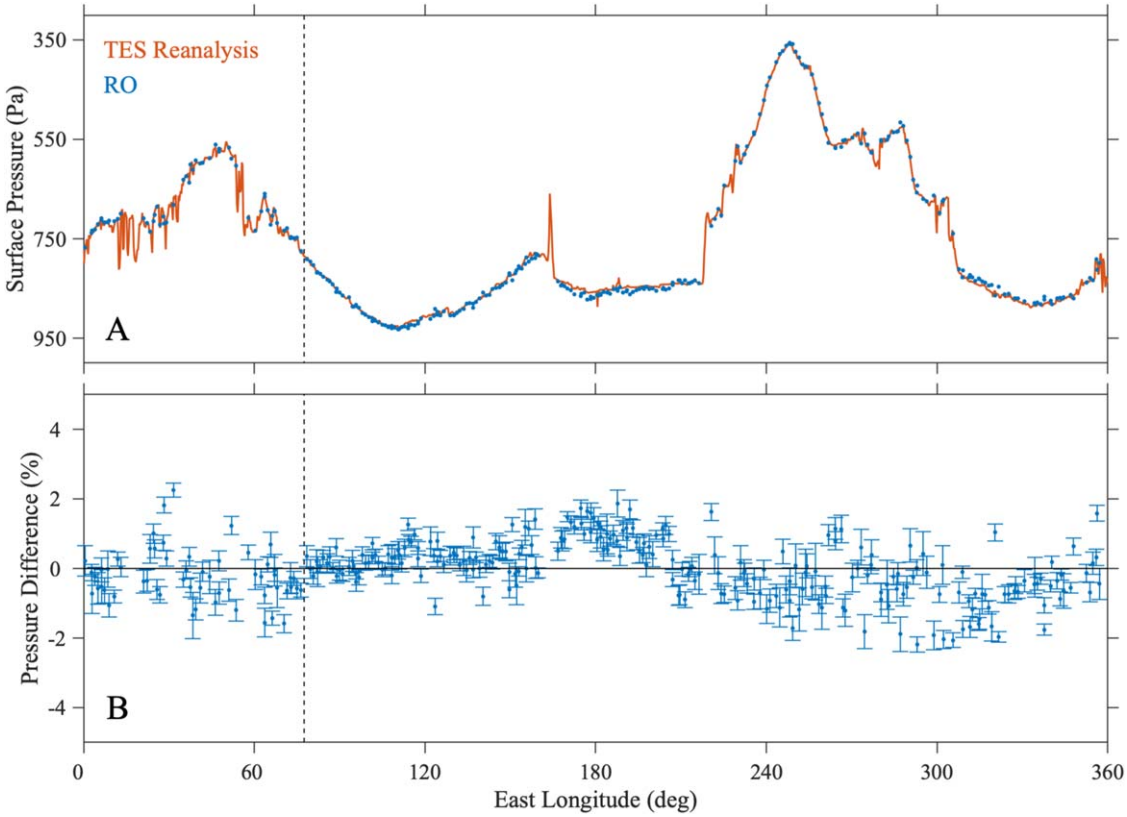

Figure 10. (A) Zonal variation of surface pressure at 37°N in mid-spring ($L_s = 40°$) of MY 27. The orange line shows results obtained through reanalysis of TES measurements, while the blue dots show independent results derived from concurrent ROs. The local time is 04:20 hr LTST. (B) The difference (RO minus reanalysis) between the two sets of pressure measurements has a bias of only 0.2% and a standard deviation of 1.0%. The error bars are the formal uncertainties in the RO retrievals. The vertical dashed line is the longitude of the landing site. The results shown here are representative of comparisons at several combinations of latitude, season, and local time.

outside major dust storm periods. This gives a small multiplicative correction to the seasonal cycle that could be applied to the surface pressure, an increase of about 0.6% (4.4 Pa) at the expected (and ultimate) time of Perseverance landing.

Surface pressure was extracted directly from the MGCM at half-hourly intervals, with the above corrections applied, at each site under consideration for landing and for periods of about 20 sols around the date of landing. One advantage of the global procedure is that a single reanalysis could be used to provide estimates of surface pressure at each of the large number of landing sites under early consideration for the Perseverance spacecraft, with relatively detailed work conducted for eight sites widely distributed around the planet.

3.4. Surface Pressure Validation

The surface pressure is tightly constrained by RO measurements. Although the data set is sparse and not sufficient for reanalysis, it provides a valuable, independent test of surface pressures derived through data assimilation. A similar approach was used previously in support of EDL for Curiosity (Vasavada et al. 2012).

The RO profiles of pressure and temperature extend from about 500 m above the surface to an altitude of about 40 km with a sample spacing of about 700 m (Hinson et al. 1999, 2014; Pätzold et al. 2016). The 1σ uncertainties in both pressure and temperature decrease from about 7% at the top of the profile to about 0.2% near the surface. The planetocentric radius of each sample in the RO profile is known to within about 10 m, commensurate with the accuracy of the spacecraft orbit reconstructions (Lemoine et al. 2001; Rosenblatt et al. 2008).

Surface pressure is obtained by integrating the equation of hydrostatic balance across the 500 m gap between the base of the RO profile and the surface. This requires a model for the temperature structure in the near-surface boundary layer, which is derived from linear extrapolation of the RO temperature profile. As the difference in pressure between the base of the profile and the surface is only about 5%, this simple model for the temperature structure of the boundary layer is expected to increase the 1σ uncertainty in surface pressure by no more than about 0.5%.

The RO profiles from both Mars Global Surveyor (Hinson et al. 1999) and Mars Express (Pätzold et al. 2016) are used to test the performance of the reanalysis of Section 3.3. Estimates of surface pressure are obtained from four groups of profiles, all from low latitudes in the northern spring season. (No RO measurements are available at the exact location, season, and local time of Perseverance EDL.) For example, one group of about 300 profiles sampled the atmosphere in mid-spring ($L_s = 40°$ of MY 27) at a local time of 04:20 hr LTST, providing complete coverage in longitude within a narrow latitude band centered at 37°N. Each RO surface pressure is compared with the corresponding result from the reanalysis; the MOLA 0°.25 resolution map of surface topography is used as the basis for all comparisons. In this case, the pressure difference between the RO measurements and the reanalysis has a bias of about 0.2% and a standard deviation of about 1.0%, as shown in Figure 10. Similar results are obtained from comparisons between the reanalysis and groups of RO

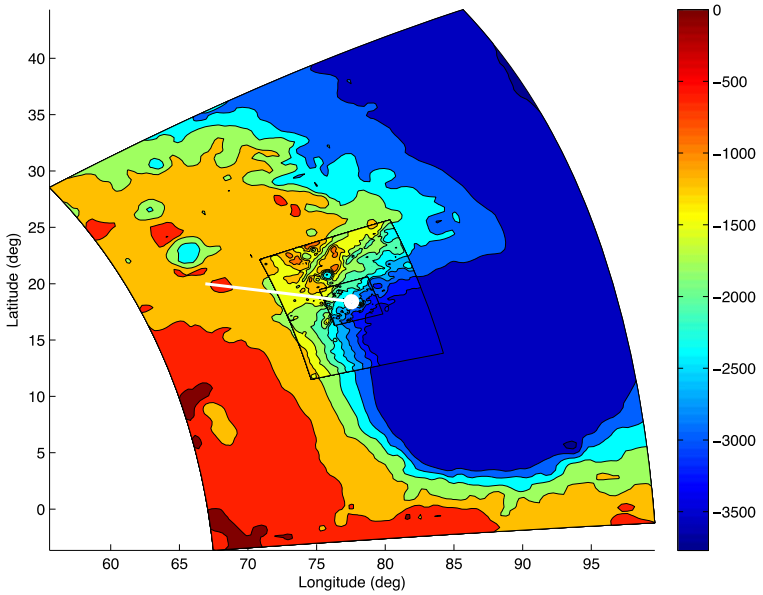

Figure 11. Elevation (in m) contour plot of the various MRAMS grids of different resolutions for Jezero crater. Note the refinement of the topographic contours within the higher-resolution grids. The Mars 2020 entry trajectory is shown in white.

profiles at other latitudes, seasons, and local times, which implies that surface pressure predictions from the data assimilation are accurate to about 1% (1σ).

3.5. Creation of "Combination" Profiles

3.5.1. Processing of the Mesoscale Data

The raw mesoscale data from the OSU MMM and MRAMS models provide atmospheric properties as 3D tables that are functions of altitude, longitude, and latitude. The spatial grid is not common between the data from the two models; additionally, both models provide grids of different resolutions (spatial and temporal) and for a different number of sols. Thus, to use the mesoscale atmospheric properties and wind speeds within the flight dynamics engineering tools, the two disparate data sets need to be combined to create one coherent set of profiles that (a) capture the inherent atmospheric properties and (b) provide statistical information for probabilistic engineering evaluation of the spacecraft performance. For Mars 2020, as with MSL, this process leads to the generation of a single combination ("combo") profile and its dispersions.

One of the first steps in creating the combo profile is to establish the grid on which to gather the data. The grids are overlapping, with the smallest grid having the highest-resolution data but smallest spatial coverage. Figure 11 shows the various resolution grids (as nested squares) supplied by the MRAMS model for Jezero crater. The trajectory of the Mars 2020 vehicle is overplotted in white. An overlay of this type allows one to select data from the proper grid for generation of the combo profile. Earlier along the entry trajectory, data are acquired from the larger grid. As the spacecraft approaches its final landing location, data from smaller and higher-resolution grids are obtained instead.

The 3D spatial grid is reduced to two dimensions by aligning the grid along the (constant) trajectory azimuth such that there is a fixed latitude/longitude relationship. The constant azimuth trajectory for Mars 2020 is shown in Figure 11. This decrease in dimension is done to reduce the size of the combo tables used by the flight dynamics simulation. Given a chosen entry trajectory, all atmospheric data from both models are interpolated to a common altitude versus longitude grid (where the latitude is treated as a function of longitude for entry). Logarithmic interpolation is used for pressure and temperature in altitude, while linear interpolation is used for all other atmospheric properties in altitude and longitude. The resulting atmospheric data on a common grid are represented schematically in Figure 12.

For each mesoscale model, the mean and standard deviation of each atmospheric property are calculated from the interpolated data obtained from all simulated sols (see Sections 3.1.1 and 3.1.2) and within a 1.5 hr local mean solar time window around the target landing time. The mean and standard deviation from each mesoscale model are then averaged to create final values for the combo profile, providing equal weight to each model. For the wind profiles, the standard deviations of the combo model are defined as a worst-case scenario so as to stress the flight dynamics simulation. The mean combo profile is still based on the average of the two mesoscale models, but the 3σ bounds of the combo wind model at each vertical grid point are independently defined as the larger extreme of either model, as seen in Figure 13.

3.5.2. Usage within Flight Mechanics Simulations

The combo profile is provided to the flight mechanics simulations as two tables (density and wind) from 125 km altitude MOLA down to the landing site elevation—for Jezero, at approximately −2.5 km MOLA. The mesoscale data are used to define the atmosphere from the landing site up to about 50 km MOLA, near the upper boundary of the models. Above the mesoscale model region, hydrostatic equilibrium and an isothermal assumption are used to define pressure, temperature, and density, while the wind speeds are linearly reduced to zero at 125 km altitude. Above 50 km, during hypersonic flight, the flight system is insensitive to wind (Cianciolo et al. 2008); the linear decay of wind is implemented as a numerical convenience to avoid a step function in the model at the top of the mesoscale domain.

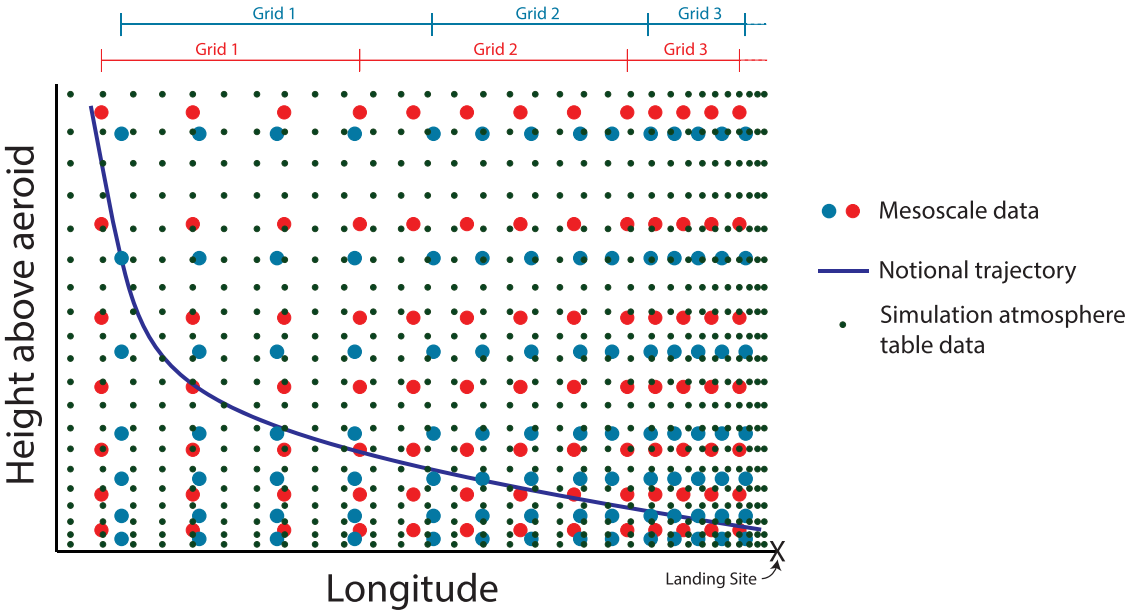

Figure 12. Conversion of mesoscale data from native grids (red and blue dots for the two different mesoscale models) to a common grid (small green dots) via interpolation in altitude and longitude while assuming that latitude is a function of longitude. The mesoscale data spacing decreases for higher-resolution nests (indicated here by a generic grid number). The grid spacing gets smaller closer to the surface and the landing site.

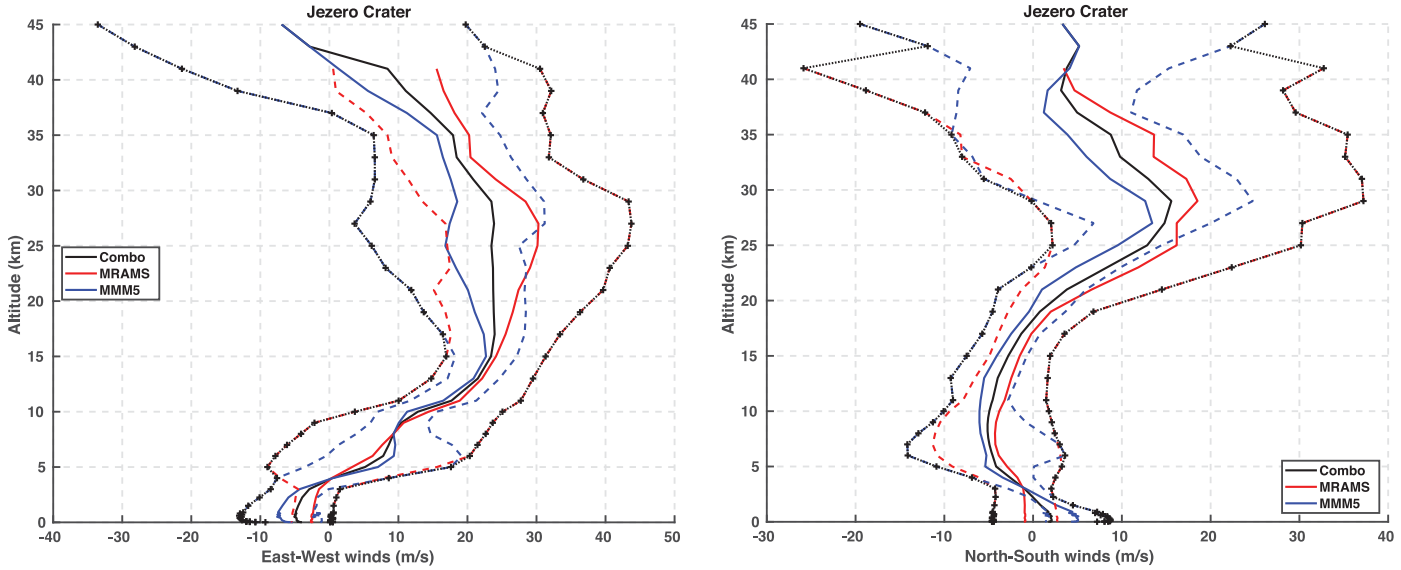

Figure 13. Combo profile for the zonal (left) and meridional (right) winds using the worst-case mesoscale wind data to define the boundary. Solid lines are mean profiles, and dashed lines are the boundaries of the dispersion. The $\pm 3\sigma$ bounds are defined as the larger value (in magnitude) of either the OSU MMM or MRAMS model at each model level.

In order to stress the flight performance of the spacecraft within the flight mechanics simulation, the atmospheric properties have further dispersions added to them. The densities from the combo profile are further dispersed by $\pm 10\%$. The wind tables are dispersed within the flight dynamics simulations in a fashion where both the mean wind (Figure 14(a)) and the dispersions (Figure 14(b)) are varied by $\pm 3\sigma$. Together, this approach produces a large envelope of wind speeds that stresses the performance of the vehicle at a level equivalent to $\pm 4.24\sigma$ (Figure 14(c)).

Based on the accumulated data from spacecraft observations, it was not expected that any substantial dust activity would be observed during EDL. Nevertheless, the CoA conducted several "contingency" experiments looking at the influence of increased dustiness (via local or regional dust storms) at Jezero during landing. These include the active dust-lifting simulations with MRAMS discussed in Section 3.1.2 and a so-called "dust bomb" simulation with the OSU MMM, whereby a large regional dust storm was prescribed to pass over Jezero crater during EDL. These simulations were defined as "dusty" scenarios by the flight mechanics team. As with the nondusty cases described above, a combo profile was generated from the two dusty scenarios so as to produce a potentially greater variability in atmospheric density and wind. The dusty combo profile is shown in Figure 15 (compare with Figure 13). For even the most extreme dusty simulations performed, however, the flight system remained well within its performance margins. Had such an extreme condition presented itself during EDL, the

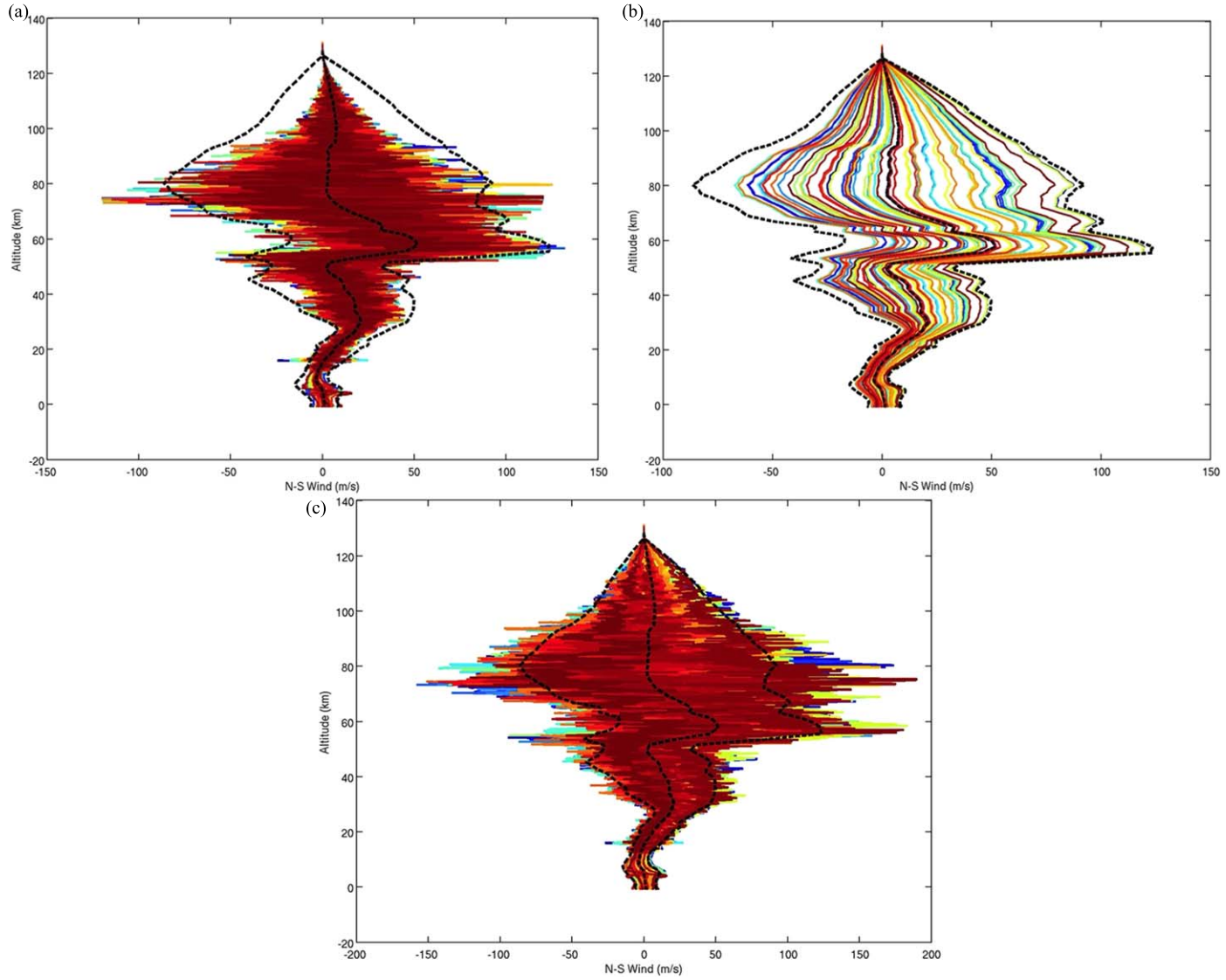

Figure 14. Approaches to introducing variations to mean and dispersed wind profiles. (a) Varying mean wind by $\pm 3\sigma$. (b) Varying wind perturbations by $\pm 3\sigma$. (c) Combination of (a) and (b). Note the different x-axis range in panel (c).

CoA was ready to deliver an updated combo profile to the EDL team reflecting the greater variance in the dusty atmosphere.

3.5.3. Further Validation against MCS Data

Figure 16 shows the comparison of the mesoscale models and combo table to the MCS profiles. Below ~50 Pa (and especially between 10 and 20 km, the zone of primary interest; see below), the comparison to the mesoscale models is quite good. The 6 yr of historical MCS profiles are essentially within the envelopes of both mesoscale models (gray and purple dashed curves). Starting at around 60 Pa and higher in the atmosphere, the MRAMS model starts to deviate from the MCS profiles, becoming significantly colder (by as much as 30 K at 10 Pa). The MRAMS profiles do not capture the decrease in lapse rate and start of the dominant wave structure. These features are closer to the upper boundary of the MRAMS model, and their absence may be partly due to the Rayleigh damping layers implemented at the top of the MRAMS domain, squelching the wave effects. The OSU MMM mesoscale model does a better job capturing the change in lapse rate and wave structure in this region, although it is somewhat colder than the MCS historical values as well. The combo profile (black dashed curves) is well centered on the historical MCS profiles up to ~50 Pa, with an ample margin. Above this height, the combo table is missing the change in lapse rate and the average wave structure. The historical profiles, including this wave structure, do approach the bounds of the combo profile at ~7 Pa; however, as noted in Section 3.5.2, the Mars 2020 EDL system is rather insensitive to conditions at these altitudes.

In comparing the mesoscale models (and ARC-MGCM) to the MCS data, there are a number of things of which to be mindful. The models are not being driven by the observations and will thus not capture the weather (or possibly even the range of weather) seen in the observations. To reduce this impact, the data are averaged over a moderate-length period (15 days) to provide a more climatologically mean condition. Also, when doing these comparisons, the MCS data are from previous years and therefore only encompass the seasonal conditions that were sampled. While the year-to-year variability is low at this season, there are only six MYs of data; thus,

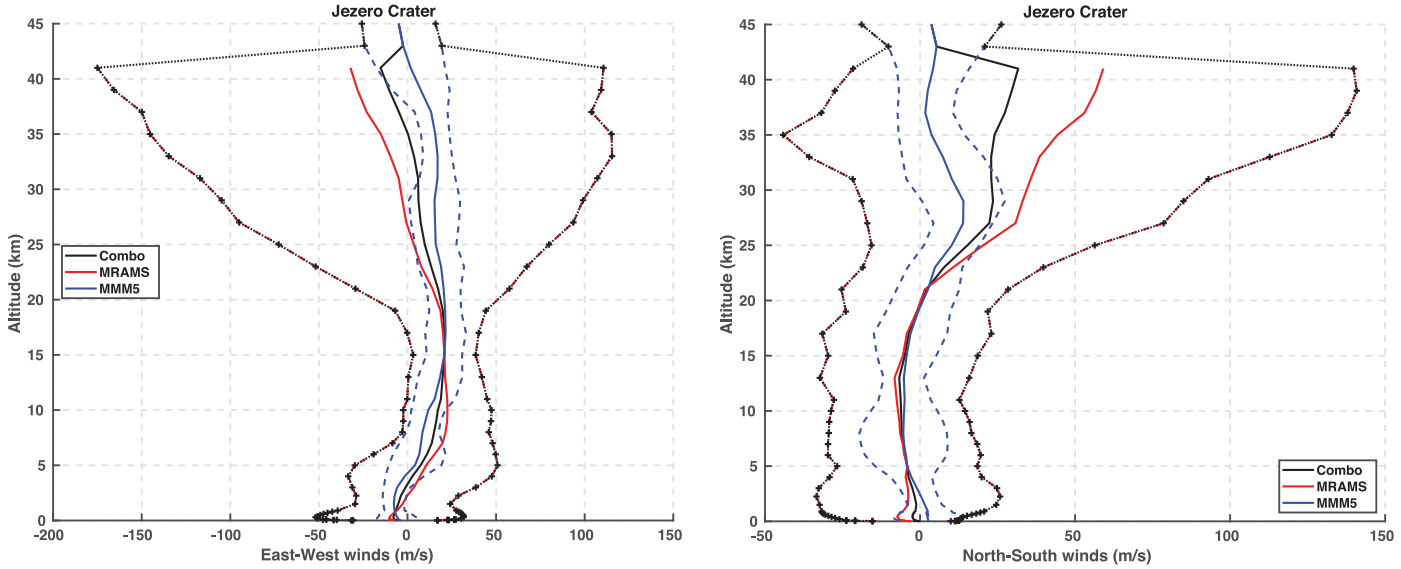

Figure 15. Same as Figure 13 but using the dusty simulations of MRAMS and the OSU MMM. Note the increased variance across much of the profile. The sharp gradient at the top of the boundary reflects the lower cutoff of the MRAMS model above ∼40 km.

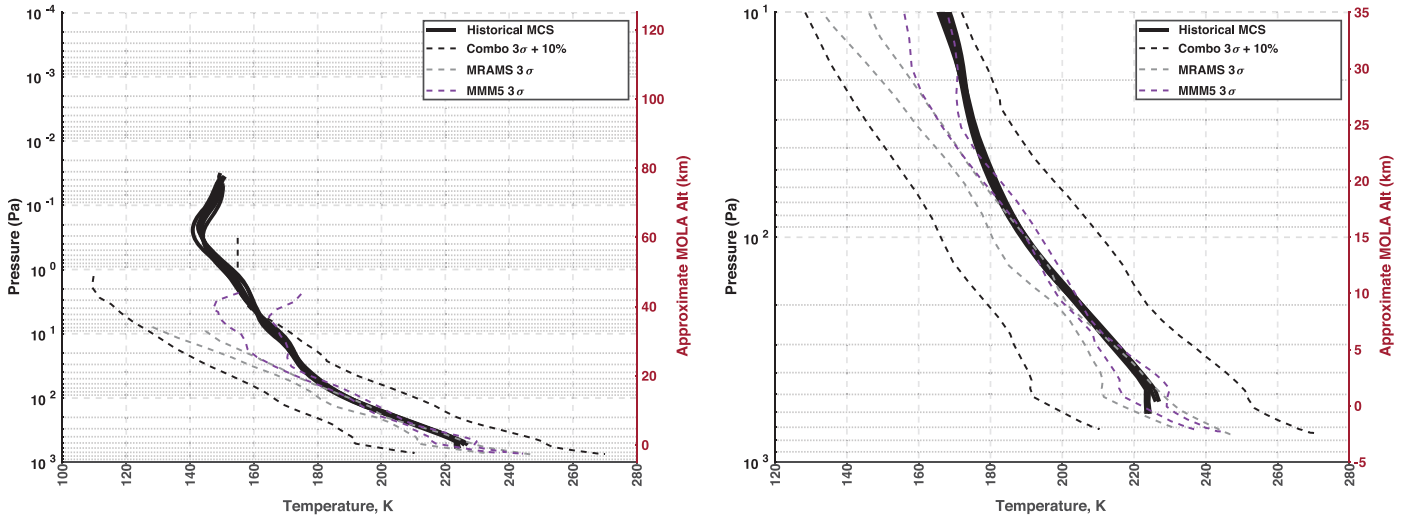

Figure 16. (Left) Comparison of MRAMS (gray dashed lines), OSU MMM (purple dashed lines), and the standard combo temperature profiles (black dashed lines) with the historical MCS observations (solid black lines) at Jezero crater at the season and local time of landing. Historical MCS data include profiles from six MYs (MY 29, MY 31–35). (Right) Detailed view from the surface to ∼35 km MOLA, the region of greatest concern for EDL.

the most extreme possible conditions may not have been observed. In evaluating the wind fields, a key concern for EDL, the temperature comparisons help with but do not provide definitive validation; it is possible for a model to generate noticeably different wind fields while still having a temperature field within the MCS measurement uncertainty.

Overall, the comparison between the mesoscale models and MCS observations ranges from very good to excellent. This is particularly the case in the vertical regions of the atmosphere of most interest for EDL. The comparisons serve as a means of model validation used to establish confidence in future analysis for Mars 2020 EDL.

3.5.4. Differences in Procedures between Mars 2020 and MSL

For the most part, the inputs and outputs of the combo profile generation process from MSL were maintained for Mars 2020; however, based on lessons learned from MSL, the following changes to the process itself were made.

1. The raw mesoscale data from each model were archived in a single place, rather than separately by the mesoscale modeling teams, as done for MSL. This streamlined the process of performing reanalysis as procedural or other changes were implemented and maintained a chain of ownership.
2. Scripts used to process both mesoscale model outputs as in Section 3.5.1 were standardized, and the same scripts were used for each. Previously, for MSL, each model used independent processing scripts that often led to discrepancies between the outputs, requiring additional time to reconcile.
3. Most significantly, adjustments were made to the Mars Global Reference Atmospheric Model (MarsGRAM 2005) code (Justh & Justus 2007) to accept the standard

deviation values of density and horizontal wind from the mesoscale models. MarsGRAM is used to feed the combo profile into the EDL simulations and add high-frequency noise to the data. Previously, instead of the model-derived standard deviations, the ratio between the combo profile standard deviation and the default MarsGRAM equivalent standard deviation at each level was used.

3.6. Real-time EDL Support

During flight operations, MCS provided sounding profiles of temperature, dust, and water-ice opacity as a function of pressure and altitude near the landing site every day around the local solar time of landing. These MCS profiles were compared to the combo profile to determine if the latter was still appropriate for the weather expected for landing. (In the unlikely event that a large storm appeared and modified the atmosphere around Jezero close to landing day, the combo profile could be adjusted based on the dustier "contingency" simulations produced by the mesoscale models.) Figure 17 shows a sample of plots analyzed during flight operations to evaluate the combo profile against MCS observations. Figure 17(a) shows individual MCS profiles (solid colors) and historical MCS profiles from prior MYs (solid black) compared against the 3σ temperature uncertainties derived from the OSU MMM (purple dashed), MRAMS (gray dashed), and combo (black dashed) models. Figure 17(b) shows similar data but converted to atmospheric density and normalized (arbitrarily) to the mean density from the MRAMS model. Between 10 and 20 km MOLA altitude, which is the region of highest spacecraft sensitivity to density, if the MCS profiles in the region of interest were inside combo $3\sigma + 10\%$ (black dashed lines), no changes would be recommended to the EDL team. If the MCS profiles were outside those bounds, the CoA would consider a revision to the combo model. As seen in Figure 17(b) (for MCS data 2 days prior to landing), the modeled atmospheres were exceptionally well aligned with the data. Throughout the approach phase of Mars 2020, no change in the combo atmosphere was required.

In addition to direct assessment of atmospheric profiles with MCS, the CoA used several other spacecraft data sources to provide information about the atmosphere in the weeks leading up to EDL. These sources are discussed presently.

3.6.1. Mars Color Imager

MARCI is a dual-head (UV and VIS) push-broom camera system on board the MRO spacecraft, which provides global imaging of the planet in seven spectral bands ranging from the UV (258 nm) to the near-IR (718 nm; Bell et al. 2009). The wide field of view (180°) of MARCI and its continuous dayside imaging provide limb-to-limb and terminator-to-terminator coverage of the planet's surface and atmosphere across each of the 12–13 orbits the spacecraft makes each day. In support of Mars 2020 EDL, the 12–13 consecutive orbital image swathes in each of the visible RGB filter bands were used to create a daily global, color map in a simple cylindrical projection at a scale of 3.75 km pixel^{-1}, which is the resolution at the limb of the MARCI image. The daily global maps were used to monitor for synoptic weather phenomena (condensate clouds and dust storms) in the same way as in previous weather studies (Cantor et al. 2001, Cantor & Malin 2002, 2010, 2019; Vasavada et al. 2012). Specific attention was given to weather events that tracked within 2000 km of the Jezero crater landing ellipse during the weeks leading up to and including the day before EDL. There was no MARCI coverage of Jezero crater the day of landing; the MARCI camera was turned off at the start of the orbit before and through the end of the orbit past Jezero crater on landing day so as to minimize any potential increase in background noise that could impact the efficiency of the Electra communications package on board MRO, which was used to monitor for a rover signal at landing.

The image of the Mars atmosphere on the day before the Mars 2020 entry (~24 hr prior to entry) is shown in Figure 18. The red dot represents the location of Jezero crater. The bright area at the top of the image is the seasonal north polar cap. Condensate clouds show up as bright and diffuse white features, and dust storms are a brownish color. Based on the interpretation of the MARCI global maps, there was no storm threat to the Jezero crater region in the 24 hr leading up to Mars 2020 atmospheric entry.

Cantor et al. (2019) reported that the probability of a dust storm passing within 2000 km of the landing ellipse in Jezero during EDL was on the order of 0.6%–1.5%, and that for 1000 km or less, it was 0.0%, based on observations from MY 28–34. The MY 36 proved to be no different, as no dust storms were observed in close proximity to Jezero crater during the week before or after EDL.

3.6.2. Mars Climate Sounder

While this study previously addressed the importance of MCS data for model comparison, a few additional words about its design and implementation are warranted. The MCS is a nine-channel radiometer with one visible/near-IR channel and eight thermal IR channels (McCleese et al. 2007). Each channel has an array of 21 detectors that are placed on the limb (or horizon) to cover from the surface to ~80 km with an ~5 km resolution. In addition, on-planet observations are acquired to provide good sounding of the lowest scale height in the atmosphere. The radiance data are inverted via a retrieval (Kleinböhl et al. 2009, 2011, 2017, 2018) to produce vertical profiles of temperature, dust extinction, and water-ice extinction versus pressure (and approximate altitude). In addition, the retrieval produces column dust and column water ice values by integrating over the vertical profile (and extrapolating a well-mixed condition to the surface for the dust; Kleinböhl et al. 2020). Profiles are obtained daily on all 13 MRO orbits (daytime and nighttime) from pole to pole from MRO's Sun-synchronous 3 am/3 pm LMST orbit (Zurek & Smrekar 2007). The MCS can also look cross-track to obtain profiles ~1.4 hr earlier and later in local time (in the tropics; Kleinböhl et al. 2013). This mode was used for acquiring some of the historical data and provided adequate local time sampling to bracket the time of day of EDL. As with MARCI, profiles at these extended local times were only acquired immediately before and after EDL (2 hr earlier or 2 hr later) during the approach support period due to the fact that MCS was powered off for EDL to avoid interference with the Electra radio. Sideways looks on the prior and subsequent orbits were attempts to sample as close as possible, spatially, to the landing site on landing day (albeit at a cost of acquiring data at earlier and later local times than EDL).

The MCS landing approach support for Mars 2020 was very similar to that planned and executed for previous missions,

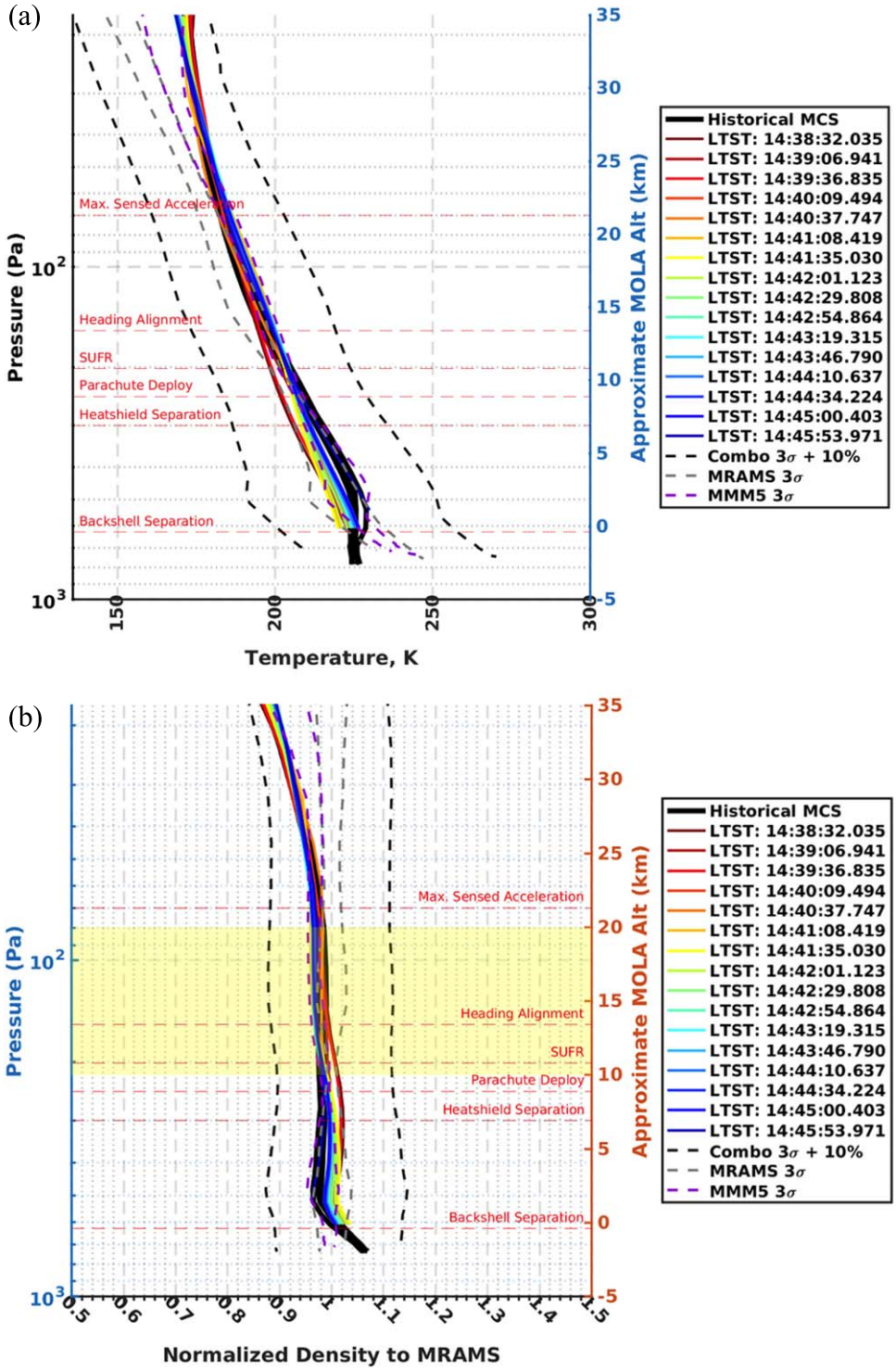

Figure 17. Examples of comparison between combo profiles and MCS data used during flight operations. (a) Comparison of raw MCS profiles from observations on 2021 February 16 (2 days before landing) and mesoscale data. (b) Comparison of MCS profiles from 2021 February 16 and mesoscale data normalized to MRAMS data. Solid colors show individual MCS profiles at the listed LTST. Solid black lines show historical MCS data from prior MYs. Dashed lines show the 3σ uncertainty ($3\sigma + 10\%$ for the combo) for each mesoscale model. The yellow shaded region between 10 and 20 km is the area of greatest sensitivity of the spacecraft to density.

including Phoenix (Tamppari et al. 2008), MSL (Vasavada et al. 2012; Chen et al. 2014), and InSight (Golombek et al. 2020). On a regular cadence (daily in the week prior to EDL), the most recent individual MCS-retrieved profiles near the landing site were examined and averaged. For this purpose, a $\pm 15°$ latitude/longitude box was used (as it was for previous missions), ensuring there was at least one MRO orbit track falling within the region and providing sufficient latitudinal coverage to understand regional trends across the landing site. Due to the smooth flow of the downlinked data through the Deep Space Network, the latency for the MCS data when they were delivered to the CoA was slightly less than 1 day. The final delivery, late in the evening on the day before landing, was optimized and had a latency of 10.5 hr.

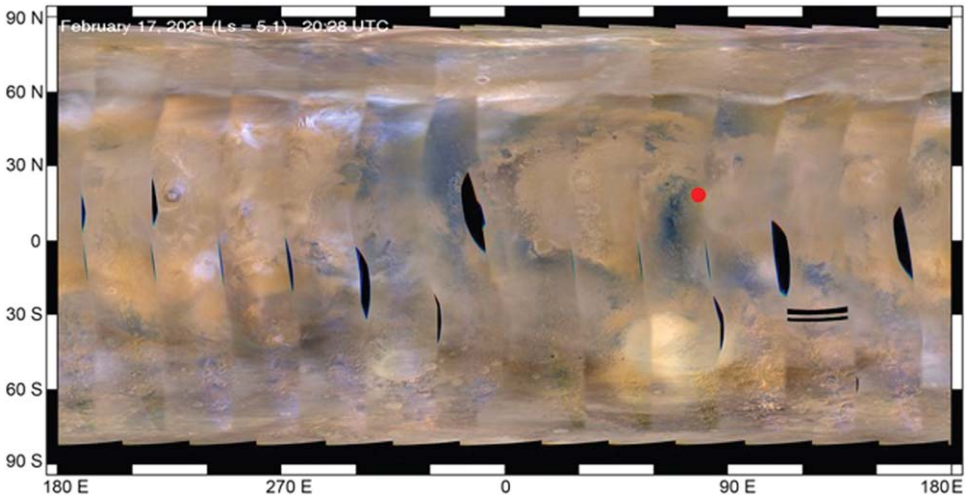

Figure 18. Daily global map of Mars for 2021 February 17, 1 day prior to Mars 2020 EDL, as taken by the MARCI camera on MRO. The location of Jezero crater is indicated by the red dot. Black regions are areas of missing data, typically because of spacecraft rotation to accommodate other instrument observations.

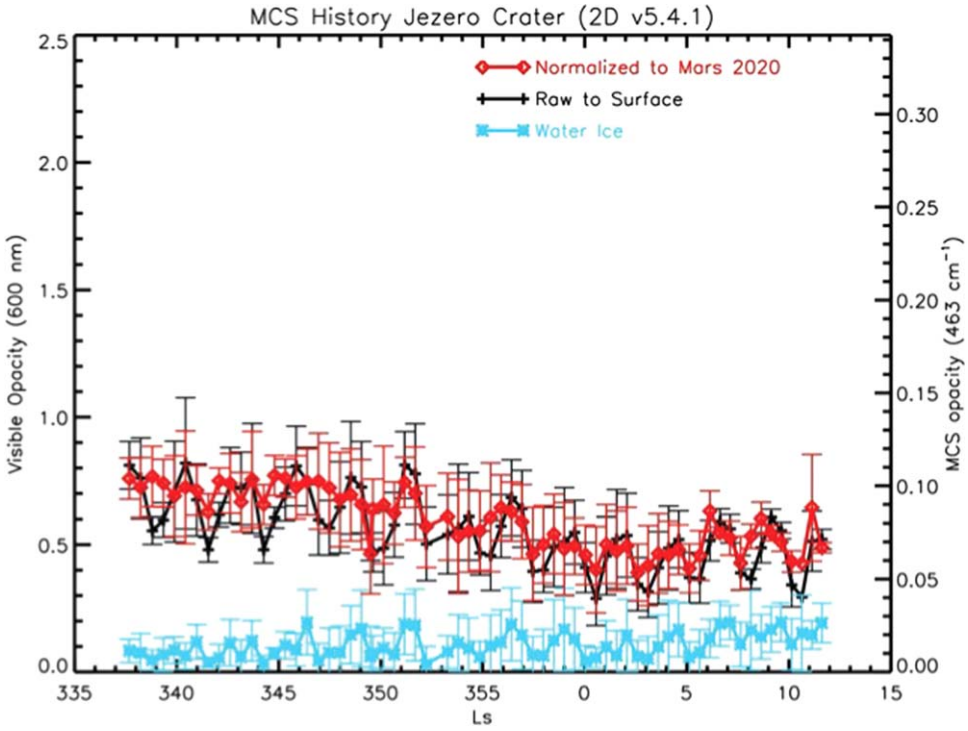

Figure 19. Dust and water-ice column opacity history in the region of Jezero crater over the period prior to EDL through to shortly after EDL, showing the expected trend of decreasing dustiness and a modest increase in water ice. The black curve shows the calculation of dust opacity to the surface at the location of an MCS retrieval, and the red curve shows the same normalized to the expected surface pressure at the Mars 2020 landing site.

There were a few minor enhancements added to the MCS processing for the Mars 2020 EDL approach support. The first change was to use MCS retrieval v5.4.1 (Kleinböhl et al. 2018) as the primary retrieval version (it had been used in a supplemental role for the InSight mission). This version of the retrieval algorithm is designed to provide improved performance in the presence of water-ice clouds, as well as extend the profiles well into the lowest scale height. This was very successful when combined with the relatively reduced cloud opacity due to the landing season and resulted in almost all profiles being successfully retrieved, as well as having several of the profiles extend to within 2 km of the surface.

To meet the delivery schedule and retain the desired ∼1 day latency, 1D profiles were used instead of standard 2D profiles. This allowed for the retrieval processing to "complete" ∼6 hr sooner and be able to process the newest profiles as soon as they arrived. It was verified with climatological data that the latitudinal temperature and aerosol gradients in the region of Jezero crater are modest at this season; thus, there was little benefit to generating 2D retrievals.

New to Mars 2020 EDL (Figure 19) was the creation of daily dust and water-ice column opacity estimates at the landing site (a preliminary version of this capability for dust was used for InSight, but it was formalized, validated, and expanded to

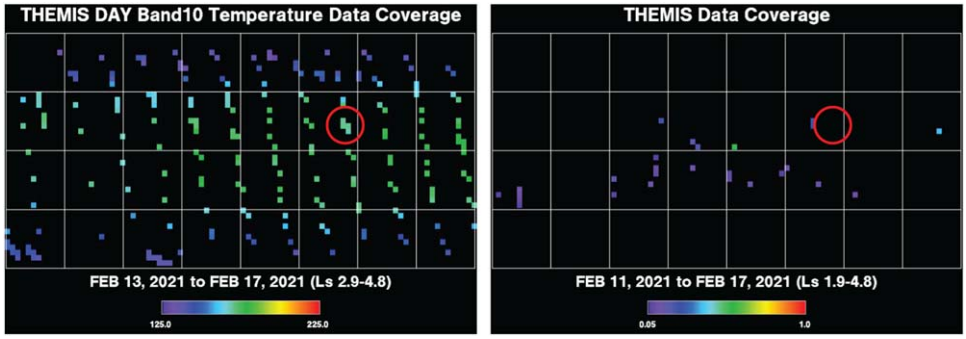

Figure 20. Sample product from the THEMIS instrument in support of real-time EDL activities. (Left) Band 10 temperature readings, accumulated between 2021 February 13 and 17 (just prior to EDL). (Right) Atmospheric opacity measurements, accumulated between 2021 February 11 and 17. Grid lines mark each 45°, with (0°, 0°) at the center of the image and Jezero crater circled.

water ice for Mars 2020). These data were provided to the EDL team to assess the need for any changes to the EDL (and, specifically, the TRN) system during final approach.

3.6.3. Other Data Sources

To provide a measure of real-time backup support in the event of an issue with either MCS or MARCI or the MRO spacecraft itself during the weeks leading up to EDL, the CoA approached other instrument/spacecraft teams who could provide relevant data on the thermal structure and opacity of the atmosphere around Jezero crater. Data were ultimately obtained from the Mars Odyssey Thermal Emission Imaging System (THEMIS) instrument, Mars Express Planetary Fourier Spectrometer (PFS), and ExoMars Atmospheric Chemistry Suite (ACS) for this purpose.

Though not designed to provide vertical profiles of temperature, the THEMIS instrument can, nonetheless, provide a "binary" assessment of atmospheric temperature using its Band 10 channel, which is a measure of broad mid-atmospheric temperatures (Figure 20, left). As the Mars 2020 entry system was generally robust to all seasonal weather conditions, the desire under these "emergency" circumstances would be only to identify the presence or absence of regional dust activity. This temperature measurement would be augmented by THEMIS IR opacity readings (Figure 20, right) to help confirm any local enhancement of dust. THEMIS coverage of the surface is limited, so temperature and dust maps provide information only about larger-scale regional storms that would last for multiple days, not brief, local storm activity. Results from THEMIS showed no enhanced storm activity around Jezero for the week leading up to EDL.

The Mars Express PFS (Formisano et al. 2005) was able to provide useful temperature profiles on an intermittent basis in the weeks leading up to EDL and a daily basis during the final week of approach, predominantly in its "spot-tracking" mode, where the instrument focuses on a single location on the surface as it passes overhead, providing multiple profiles as a function of time (Figure 21). The footprint of PFS observations was ~300 km across; thus, individual returns smooth out the effects of local topography and surface conditions. Further, the highly elliptical orbit of Mars Express leads to an irregular time of day for periapse; the profiles obtained closest in time to landing day were at ~7:15 am local time and therefore not directly comparable to MCS profiles (taken at a mean time of 14:42:11 LTST; see Figure 17). Earlier observations by PFS were obtained at times more directly comparable to MCS, and a comparison between the two showed that PFS could serve as a satisfactory backup for MCS, if necessary. A similar comparison between PFS and MCS had previously been demonstrated for the Phoenix lander (Mischna et al. 2008).

Anticipated near-real-time results from the ExoMars ACS instrument could not be acquired due to the premature end of life of the TIRVIM cryocooler in 2019 December. The ACS team, however, delivered temperature profiles (footprint ~20 km) around Jezero crater for the EDL season ($L_s = 0°$) in the prior year (MY 35), which provided the EDL team with an additional perspective on the expected conditions for landing (Figure 22).

As with the PFS observations above, the available ACS measurements at Jezero crater were at a different time of day (~5:15 pm local time) from the MCS Sun-synchronous orbit and not directly comparable. Nevertheless, the profiles provided were in a family with other observations and model output and demonstrated utility as a backup data source.

While the MRO spacecraft performed as expected during EDL, and the CoA did not need to rely on the backup sources of data, they nevertheless provided the team with a valuable means of go-to support and were considered an indispensable component of CoA activities, reviewed daily along with the primary MCS and MARCI data.

4. Postlanding Activities

Following landing, an "as-flown" atmospheric profile was assembled to gauge the environmental conditions experienced by the spacecraft during flight. There was no instrumentation on board the spacecraft that directly measured the atmospheric conditions. Instead, a mix of preflight, indirect onboard, and postflight data were used to generate the as-flown profile. Table 1 summarizes the data sets and regions of applicability used to compile the postflight estimate of the atmosphere.

4.1. Upper Atmosphere Reconstruction (70–125 km)

The Mars 2020 atmospheric model used for simulations starts at approximately 125 km MOLA. As noted in Section 3.5.2, the upper atmosphere of the combo model, from the top down to ~50 km MOLA, assumes hydrostatic equilibrium with an isothermal temperature profile. In the reconstruction, the top of the mesoscale data serves as the lower boundary of the upper atmosphere. The MSL reconstruction used a similar process for the upper atmosphere using the MCS data at 60 km altitude to anchor the hydrostatic equilibrium integration up to 125 km (Chen et al. 2014). For

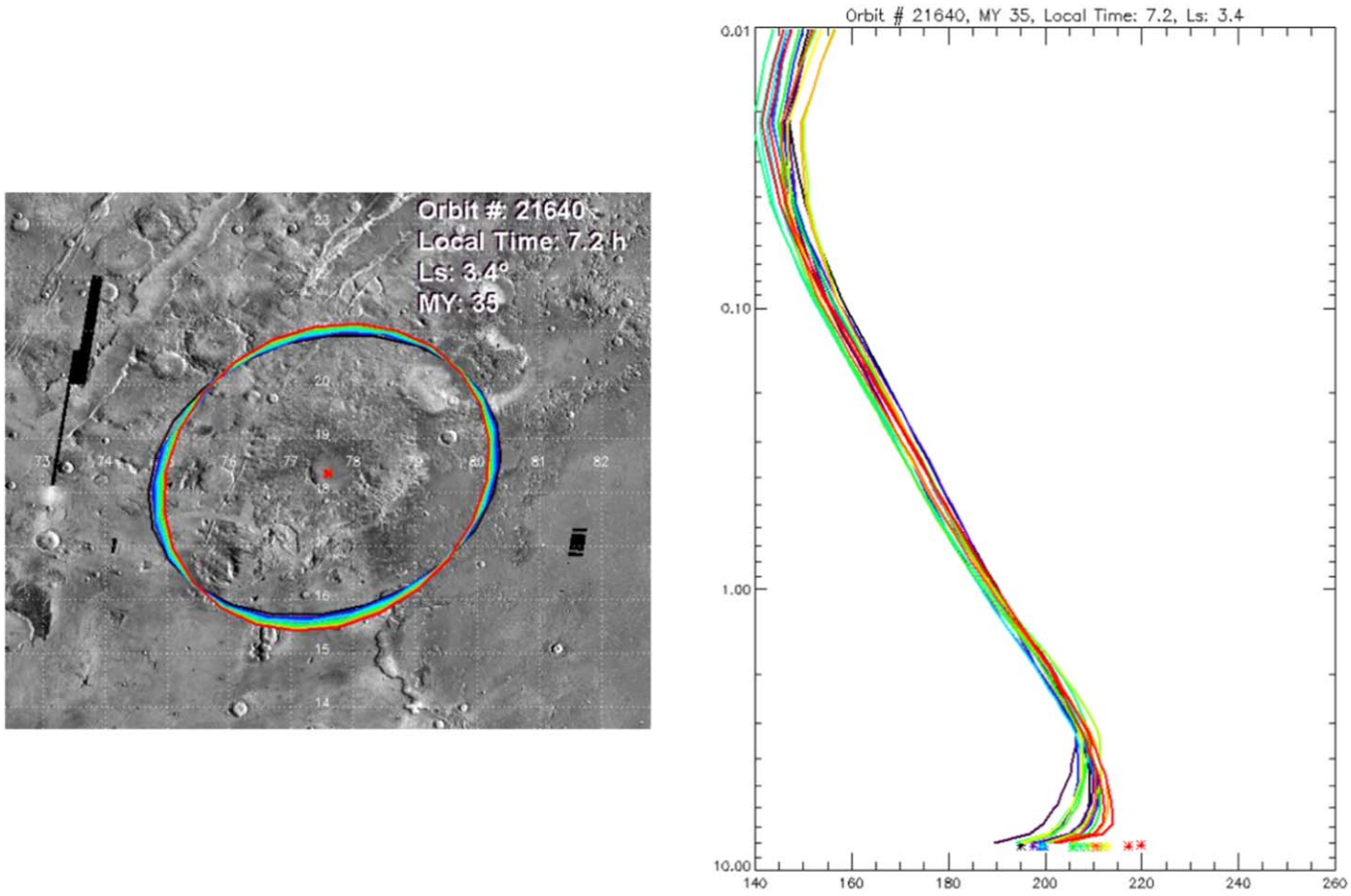

Figure 21. (Left) Image of Jezero crater with the center of the PFS observation "spots" within Jezero crater and instrument footprint. (Right) Temperature profiles obtained from PFS measurements. These measurements were obtained on 2021 February 14, 4 days prior to EDL.

Mars 2020, the postflight atmospheric data set once again does not have any data at altitudes as high as 125 km, but the MCS profiles are valid up to ∼90 km MOLA; so, for the upper atmosphere, MCS data are used for the reconstruction from ∼70 to 90 km MOLA. Since there were no MCS data acquired during the time of EDL, the postflight estimate of the atmosphere was based on the MCS profiles closest in time to landing, taken at latitude and longitudes close to the trajectory of the Mars 2020 vehicle. (The MCS data were acquired ∼2 hr before and after EDL near Jezero crater but with a 2 hr offset in local time at Jezero.) The focus was on profiles taken in locations proximal to the upstream portion of the trajectory, covering events like entry interface (EI) and guidance start.

Figure 23 shows the locations of MCS observations used to estimate the upper atmosphere along with the as-flown trajectory of the Mars 2020 vehicle. The MCS data, labeled "ATM009," "ATM010," "ATM014," and "ATM018," represent data taken at landing minus 6 days (L – 6), L – 5, L – 1, and L + 5, respectively. Fifty-four profiles with good on-planet views were chosen, as these profiles best constrained the surface pressure and allowed calculation of the pressure at the bottom of the upper atmosphere region, assuming hydrostatic equilibrium. Density was derived using retrieved pressure, temperature, and the equation of state. Wind estimates were not made for this region, as there is little interaction between the spacecraft and wind at these altitudes. Above 90 km, the atmosphere is assumed to be isothermal due to a dearth of valid data, MCS or otherwise.

4.2. Middle Atmosphere Reconstruction (10–70 km)

The middle atmosphere, for purposes of the atmospheric postflight estimate, consists of the region from 70 km down to 10 km MOLA, where parachute deployment occurred. The middle atmosphere is the only region where there are onboard data available from the Mars Entry Air Data System (MEADS) pressure ports on the forebody of the vehicle. The MEADS-based reconstruction can be briefly summarized as a weighted-average fit of the atmospheric state variables to all of the pressure port data. The four atmospheric state variables are angle of attack, sideslip angle, dynamic pressure, and static pressure (Karlgaard et al. 2014). The inertial measurement unit (IMU) data are used to reconstruct some trajectory and atmospheric relative quantities, such as Mach number, which, in turn, aid the weighted-average estimate of atmospheric properties such as the static pressure. With dynamic pressure and trajectory estimates, the free-stream density can be calculated assuming hydrostatic equilibrium. Temperature is then computed using the ideal gas law.

There is an approximately 20 km altitude overlap, from 50 to 70 km, where both MEADS and MCS data are available as postflight estimates. Both MEADS and MCS have associated uncertainties, and a weighted-average filter with the uncertainties as weights is used to blend the data estimates in this overlapping region.

The MEADS data, when combined with IMU-based velocity estimates, can, in principle, be used to reconstruct components

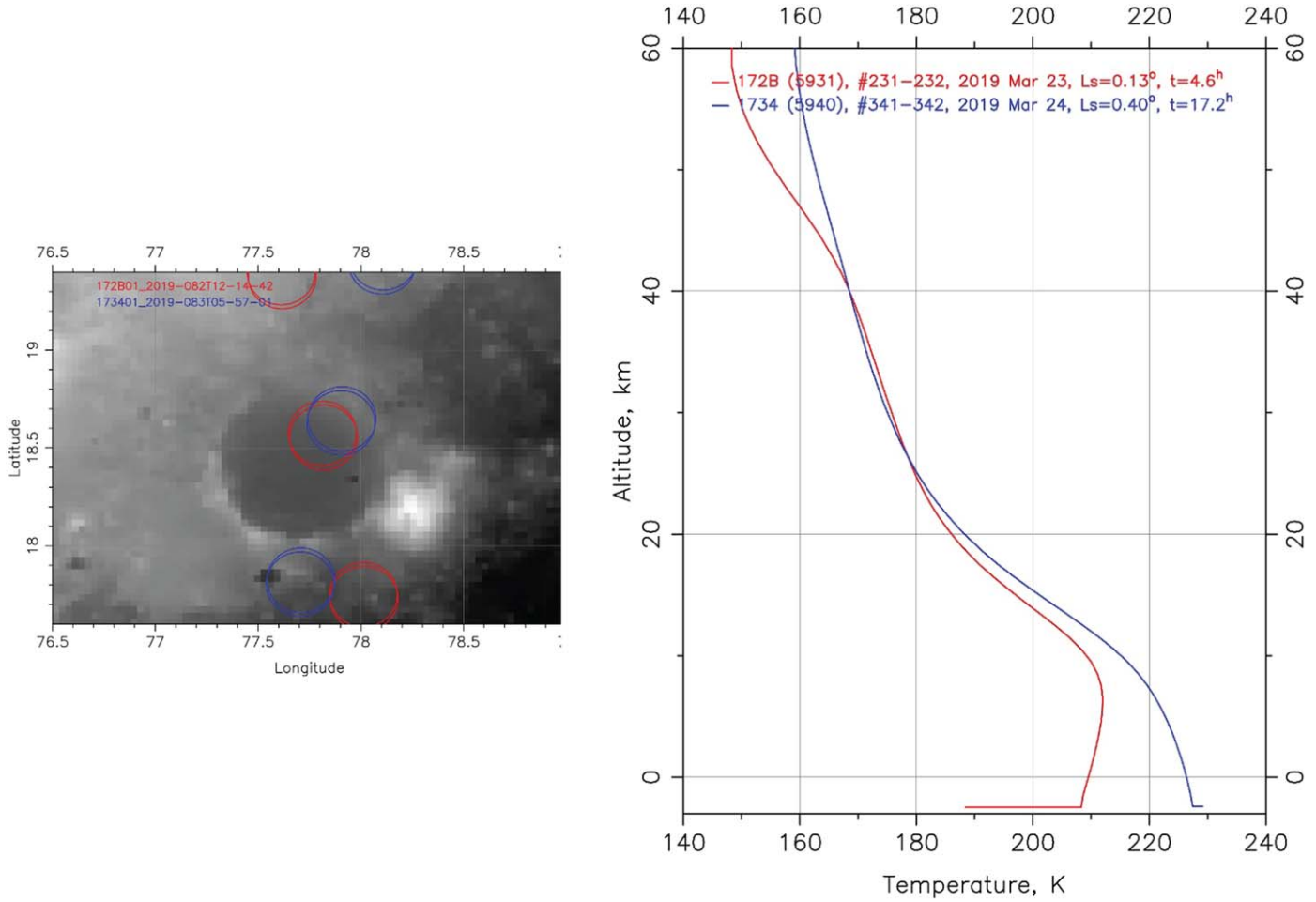

Figure 22. The ACS observations of Jezero crater around the Mars 2020 EDL season but in MY 35. (Left) Instrument footprint mapped against Jezero crater. (Right) Temperature profile for AM (red) and PM (blue) orbits.

Table 1
Data Set Used for Mars 2020 Atmospheric Profile Compilation

Data Set	Region of Applicability	Description
MCS near day of landing profiles	Approx. 50–90 km MOLA	MCS profiles taken near the locations the spacecraft traversed from L – 5 to L – 1 day
MEADS	Approx. 70–10 km MOLA	Pressure port measurements from the forebody of the heat shield, which were used to reconstruct the free-stream conditions
Preflight combo profiles	10 km MOLA down to surface	Combo profiles using mesoscale data used for temperature estimate during parachute and powered flight
MEDA instrumentation	Surface	Pressure measurement from instrumentation on the rover; data taken several days postflight

of the wind field (Karlgaard et al. 2009), though the wind reconstruction from MEADS is not currently being used for the present reconstruction; only the reconstructed pressure, temperature, and density are included from the MEADS data.

4.3. Lower Atmosphere Reconstruction (Surface–10 km)

Below the parachute deployment altitude (∼10 km MOLA), the MEADS measurements are less accurate. However, there are no other onboard measurements of the atmospheric state during parachute flight and the powered descent portion of entry. The Mars Environmental Dynamics Analyzer (MEDA) instrument (Rodriguez-Manfredi et al. 2021) is on board the rover and makes atmospheric observations but does not take its first measurement until several hours after landing. Thus, preflight data from the combo model are used to complete the lower atmosphere reconstruction. The MEDA data do provide an estimate of the pressure on the surface from observations made close to the landing local true solar time a few days after landing (see Section 5.3). This pressure measurement is integrated up to the last accurate MEADS data, assuming hydrostatic equilibrium and the preflight combo temperature profile. The preflight mesoscale data compared very well to the MCS profiles during the week prior to EDL, so the combo model temperatures are taken to be accurate in the lower atmosphere region. Given the absence of other data (MCS data typically do not consistently get down into this region), the preflight model temperature profile is therefore used in the postflight atmospheric estimate. Refinements to the lower atmosphere can also potentially include incorporation of profiles of temperature and pressure from a future GCM reanalysis (e.g., with the LMD-UK GCM discussed in

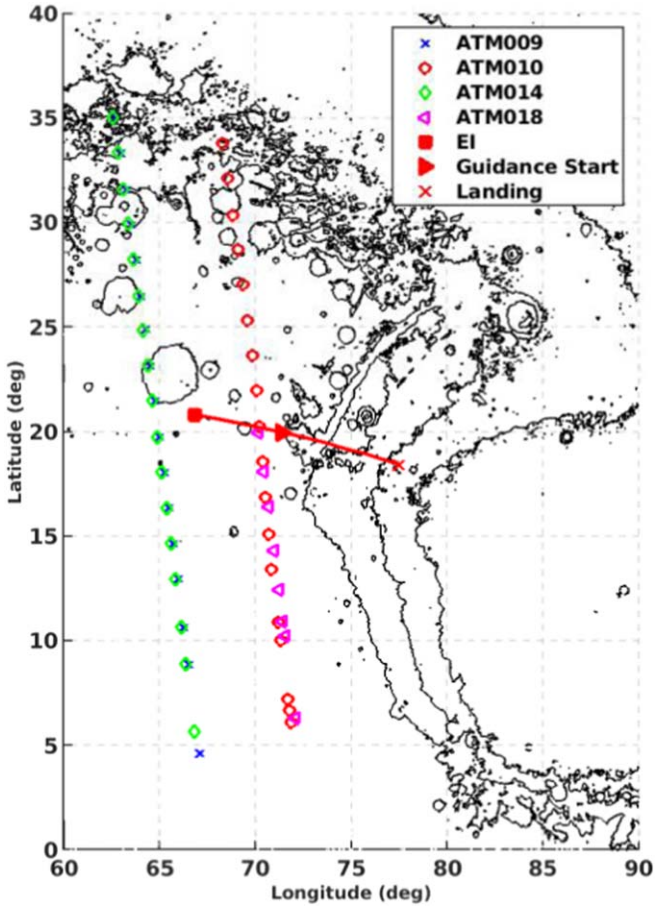

Figure 23. Locations of MCS data used for postflight atmospheric analysis and the Mars 2020 trajectory. Black contours show local topography.

Section 3.3) or even available in situ observations, such as from MEDA. It is not expected, however, that such refinements will substantially revise the atmospheric reconstruction.

5. Pre- versus Postlanding Assessment

5.1. Comparison of Pre- and Postflight Profiles

Figures 24–28 show the postflight compiled atmosphere (density, temperature, pressure, and zonal and meridional wind profiles, respectively) that has been used for reconstruction activities. The wind profiles in Figures 27 and 28 are preflight model estimates, placed here for completeness. Winds are not directly observable by any onboard data, and the MEADS-based wind estimates are not incorporated into the reconstruction, so no postflight wind profiles are presently available.

The reconstructed temperature profile (Figure 25) shows a peculiar feature at ∼14 km and another between ∼42 and 52 km that are not seen in the preflight model estimates. These are known artifacts of the postflight analysis of MEADS data and are not real atmospheric structures. Similar features in as-flown temperature estimates have been observed in past Mars mission reconstructions (e.g., Phoenix, Karlgaard & Tynis 2019, and InSight, Karlgaard et al. 2021), though the root causes for these features have yet to be identified. Regardless, the effect of this artifact on the integrated pressure and density profiles, which are more significant for the entry vehicle, is minor. Separately, the upper portion (above 50 km) of the middle atmosphere temperature excursion has an additional minor contribution due to the overlap and blending of MEADS and MCS data and their uncertainties in this narrow region.

5.2. High-altitude Atmospheric Discrepancy

Figures 24 and 26 show the compiled density and pressure profiles, along with the preflight estimate and (for pressure) historical MCS averages from multiple prior MYs during the landing season. The main observable difference is the under-prediction of the density and pressure profiles at altitudes above 40 km MOLA. Recall that for the preflight combo atmosphere, pressure and density were predicted at altitudes above 50 km using hydrostatic equilibrium and an isothermal profile, as the flight performance of the spacecraft is not sensitive to atmospheric properties above 50 km MOLA. In flight, Mars 2020 started its entry guidance 4 s before the predicted time. Entry guidance starts with an acceleration-based trigger. From Figures 24 and 26, one can see that the observed density and pressure, which were greater than the preflight prediction, may have contributed to this early start.

Another discrepancy seen in the flight performance was a lower-than-expected peak acceleration sensed by the vehicle. Peak deceleration occurs around 30 km MOLA, which falls within the region where the mesoscale models are valid. Examining Figure 17, it can be observed that, between 30 and 35 km MOLA, the MCS profiles show slightly different pressure and temperature trends than the mean of the combo profile. The OSU MMM and MRAMS models that make up the combo profile show slightly divergent behavior, with one model showing a cooling atmosphere and another showing a more isothermal profile in this region. The MCS profiles in the week leading up to EDL agreed slightly better with the OSU MMM model, but the combo profile, by design, does not weigh one model more than the other. Different scale heights and lapse rates between the two models can lead to differences in the predicted sensed acceleration.

5.3. Comparison to MEDA Data

Figure 29 compares the surface pressure predictions with measurements shortly after EDL by the MEDA instrument (Rodriguez-Manfredi et al. 2021). The reanalysis (Section 3.3) correctly predicts the time–mean surface pressure, implying that the seasonal cycle and other long-term variations are represented accurately. The day-to-day (weather) variability of the MEDA measurements is comparable to the standard deviation computed from 40 sols of reanalysis (gray shading). At this time of year, the diurnal variations in surface pressure are considerably larger than the day-to-day variability. The assimilation captures the timing and relative magnitudes of the two main pressure peaks at 08:00 and 20:00 LTST, which implies that the diurnal and semidiurnal tides are well represented. However, there are significant discrepancies of about 10 Pa between the reanalysis and the measurements at local times of 03:00 and 14:00 LTST, suggesting that a higher-order tidal mode is too prominent in the assimilation. At 15:15 LTST, when Perseverance landed, the difference between the surface pressure prediction and the MEDA observations is only a few Pa, comparable to the day-to-day variability.

5.4. Lessons Learned

Although Section 5.2 shows two places where the pre- and postflight atmospheres diverged, it should be emphasized that

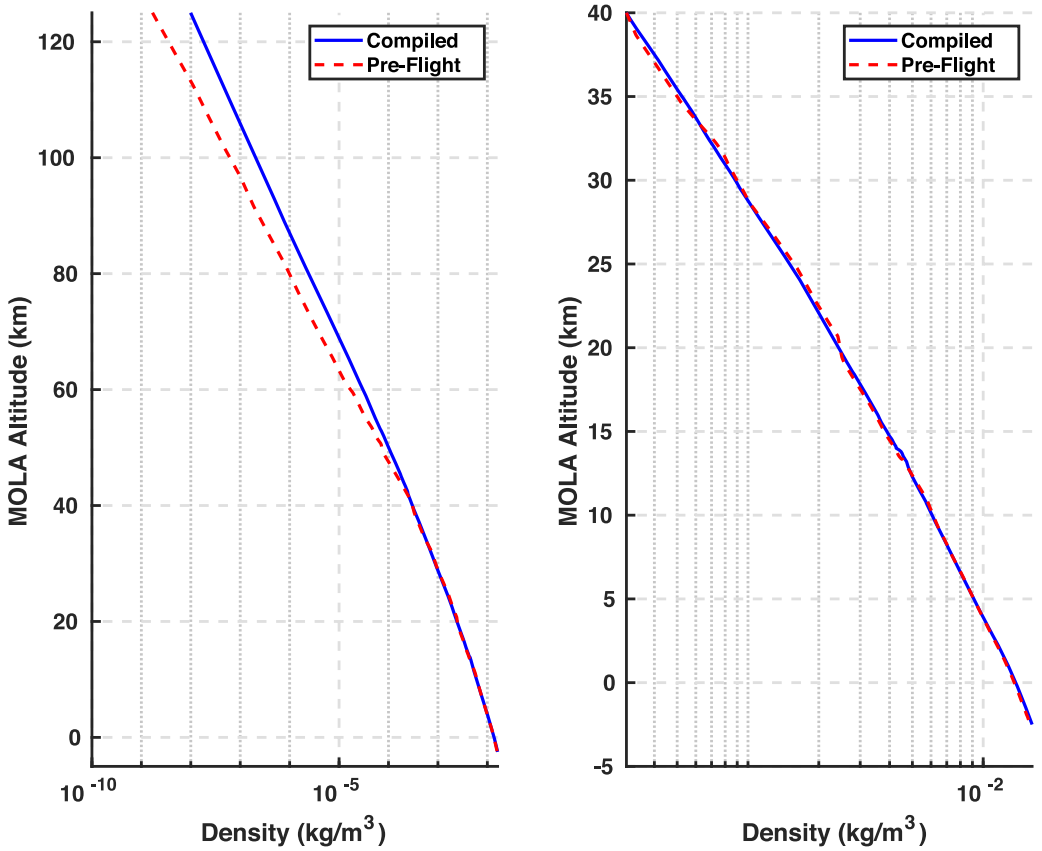

Figure 24. Postflight compiled density profile (blue) compared to preflight nominal estimate (red). (Left) Full column profile from 125 km MOLA to the surface. (Right) Enlarged view of the lower atmosphere from 40 km MOLA to the surface.

in most of the region where flight performance is sensitive to atmospheric properties, i.e., below 45 km MOLA, the preflight models agreed very well with both the MCS profiles from the week prior to EDL (Figure 17) and the atmosphere derived from postflight analysis using independent data. Mars 2020 landed during a very typical Martian spring day, supported by the fact that the daily MCS profiles analyzed during operations were regularly in the middle of the preflight model estimates. The CoA, based on their flight rules, never had to consider a change to the atmospheric model used to assess flight performance.

However, the discrepancies with the early guidance start—a feature also noticed with MSL EDL (Chen et al. 2014)—and lower-than-expected sensed acceleration suggest some changes should be made for future preflight upper atmosphere estimates. The historical MCS profiles, which were available preflight, showed that the preflight estimates were predicting lower densities and pressures (Figures 24 and 26), especially toward the top of the valid MCS region, where the preflight profile was not grounded in model data. The preflight combo profiles should have been adjusted above the mesoscale region to use the historical MCS temperature profiles instead of assuming an isothermal atmosphere. Both MSL and Mars 2020 predicted a lower density at entry guidance, and removing the isothermal assumption for the upper atmosphere could make the preflight estimates reconcile with MCS data while still using data from mesoscale models for the lower atmosphere.

The discrepancy of the lower sensed acceleration points to a need to pay greater attention to the assumptions inherent in the mesoscale models at the top end of their valid domains. It also highlights the value of using multiple mesoscale models in the atmospheric assessment. There is no easy way to assess a priori that a particular day's weather forecast from a mesoscale model will be "good" or "bad"; such is the chaotic nature of atmospheric motion. A single mesoscale model could yield a good forecast (as did one model here, for Mars 2020 EDL) or a less-good forecast (as did the other). By averaging the two models together, the net result avoids the worst scenario and the worst possible consequences.

6. Summary

With the successful landing of Perseverance in Jezero crater on 2021 February 18, the activities of the Mars 2020 CoA largely came to a close, having produced a remarkably good prediction of atmospheric conditions at Jezero through the use of numerical models and spacecraft observations. The CoA activities followed the framework used for prior missions but incorporated new approaches where warranted and leveraged the benefits of several additional years of atmospheric observations. The Mars 2020 CoA continued to use two distinct mesoscale models to form the basis of its understanding of the regional atmosphere—an approach that reduces concerns of model bias and/or error—and recommends such an approach for future EDL activities, including the forthcoming Mars Sample Return missions, which will return to Jezero crater in the next decade.

The present work had the good fortune of working with the large MCS data set, both historical and current, which served as a baseline against which the numerical models could be evaluated. The limited coverage of MCS is necessarily

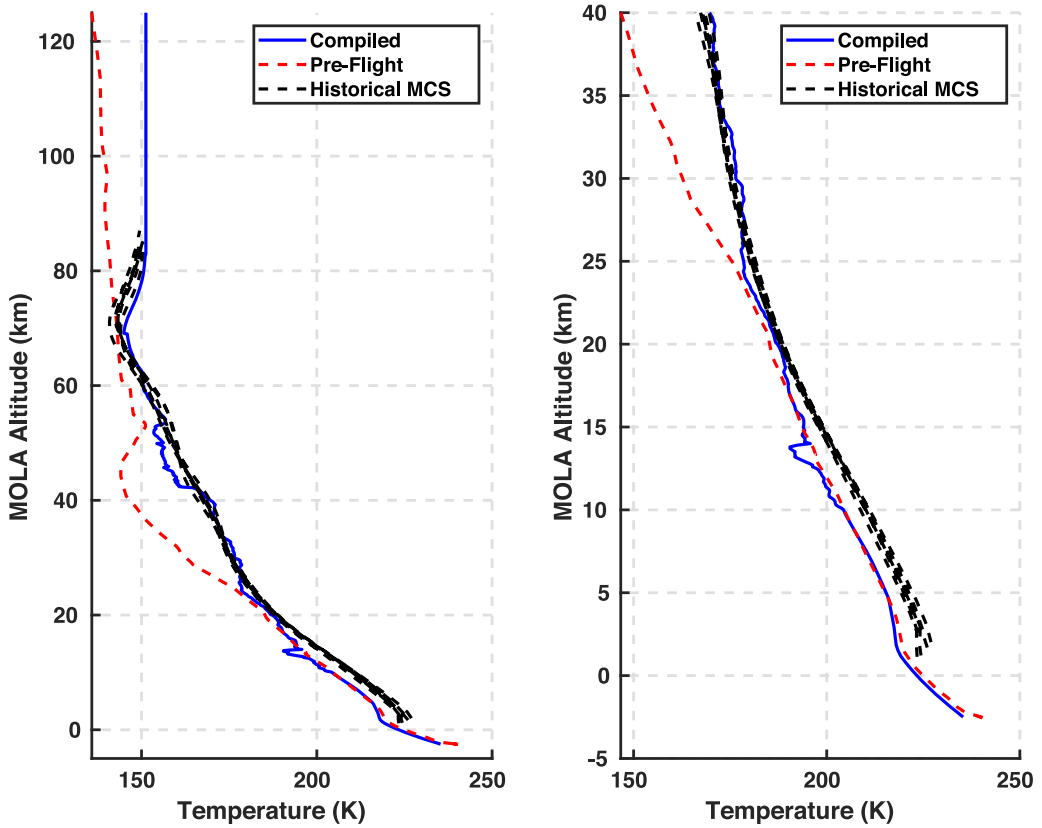

Figure 25. Postflight compiled temperature profile (blue) compared to preflight nominal estimate (red) and historical MCS data (black) at the Jezero location and EDL season from prior MYs. (Left) Full column profile from 125 km MOLA to the surface. (Right) Enlarged view of the lower atmosphere from 40 km MOLA to the surface.

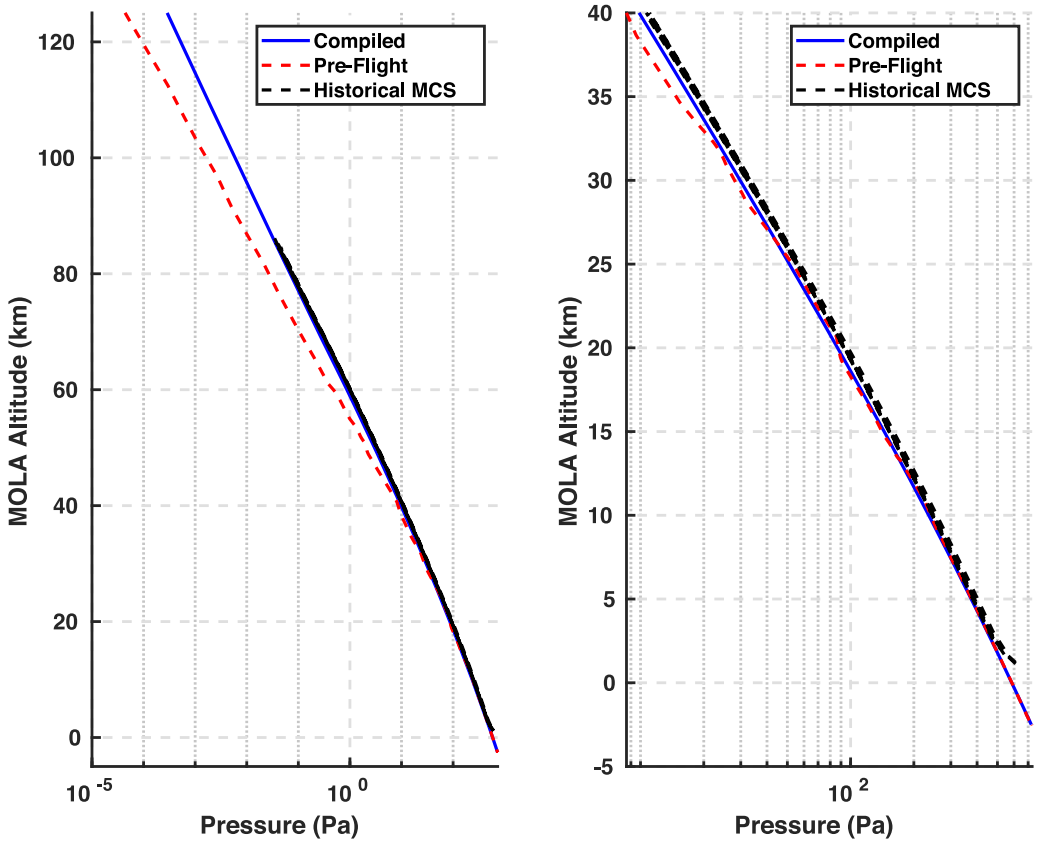

Figure 26. Same as Figure 24 but for pressure and including historical MCS data (black).

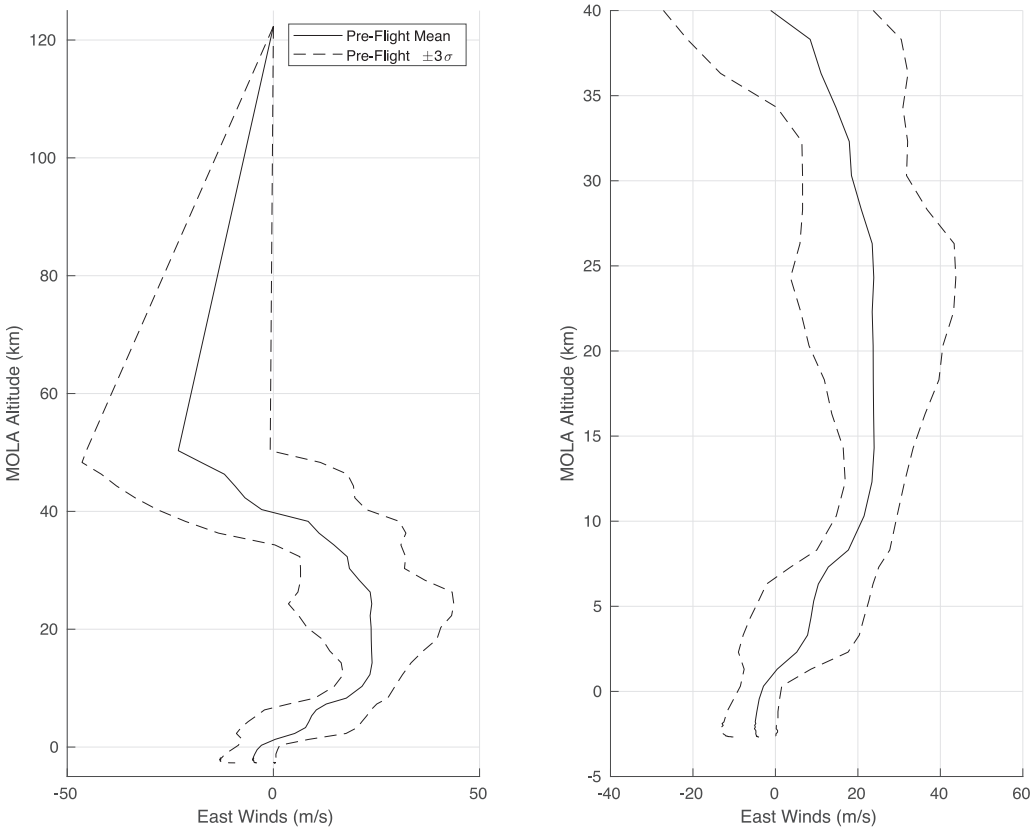

Figure 27. Preflight zonal wind predictions at the target landing site. (Left) Full column profile from 125 km MOLA to the surface. (Right) Enlarged view of the lower atmosphere from 40 km MOLA to the surface. Note the assumption of linear decay in the wind from 50 km to the top of the profile at 125 km.

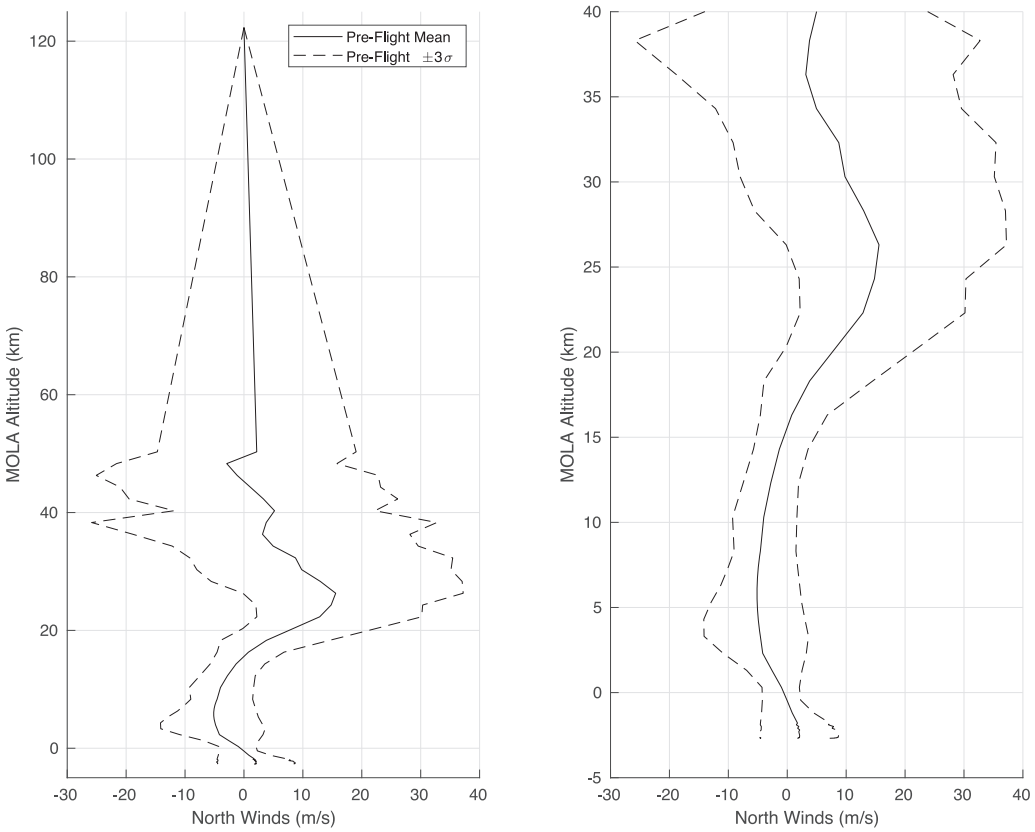

Figure 28. Same as Figure 27 but for meridional wind.

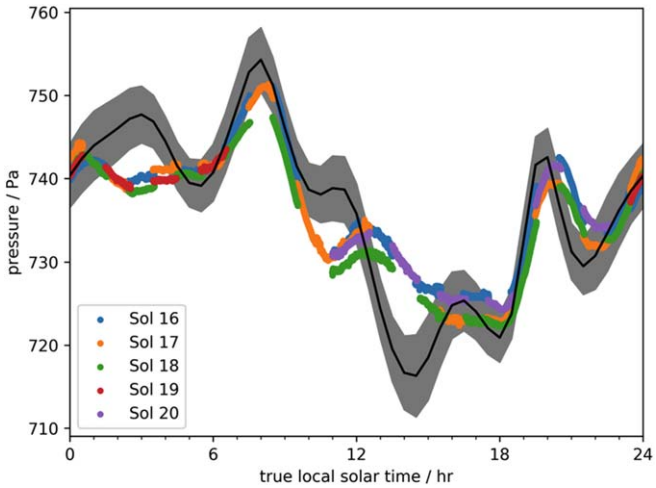

Figure 29. Predicted and measured surface pressures at the landing site in Jezero crater. The predictions (gray shaded region) are based on 10 sols of data centered on the Perseverance EDL ($L_s = 5°$) from each of 4 yr (MY 29–32). The black line is the average of the reanalysis in these 40 sols, and gray shading shows the standard deviation. The colored dots show MEDA data from sols 16–20 (relative to EDL); MEDA observations from earlier sols (not shown) are sparse and require further calibration.

augmented by the models; the combination of the two approaches is essential for a thorough assessment of the atmosphere, augmented with visual data about dust storm frequency from the MARCI camera and RO data to further refine the model output. Together, this general approach has now been successfully applied to the six most recent Mars landings (Spirit, Opportunity, Phoenix, MSL, InSight, and Mars 2020) in an increasingly refined fashion.

Lastly, this work underlines the value of regular observational coverage by a weather camera and a thermal radiometer, such as MARCI and MCS, for EDL support and suggests that such a capability should be preserved for future EDL campaigns, such as Mars Sample Return. However, future circumstances may result in more limited or an outright absence of observational data from a primary source (e.g., MCS); hence, it is good practice to seek alternate sources of data to validate the model output. The CoA considers itself fortunate to have been able to call upon the community to receive supporting data from four different spacecraft and five different instruments. The collegiality and collaboration here should serve as a benchmark for future efforts as we collectively continue to explore the Red Planet.

A portion of the work of Scot Rafkin, Daniel Tyler, Jeffrey Barnes, and Bruce Cantor was supported by the Critical Data Products Program of the Jet Propulsion Laboratory, California Institute of Technology. The work of Michael Mischna, Gregory Villar, David Kass, and Armin Kleinböhl was carried out at the Jet Propulsion Laboratory, California Institute of Technology, under a contract with the National Aeronautics and Space Administration (80NM0018D0004). We wish to thank Kimberly Murray, Jonathon Hill, Michael Smith and the THEMIS team, and Oleg Korablev and Nikolay Ignatiev and the ACS team for their support for real-time landing activities. We acknowledge the contributions of Marco Giuranna, Paulina Wolkenberg and the PFS team, and the ESA Science Ground Segment and Flight Control teams for the successful implementation and execution of the PFS spot-tracking observations over Jezero crater. We also thank Bojan Ristic, Frank Daerden, and the ExoMars NOMAD team for their enthusiastic interest in also supporting Mars 2020 EDL. We gratefully acknowledge the MEDA instrument team for providing the atmospheric data that were used to compare against the reanalysis. Lastly, we thank two anonymous reviewers for their suggestions to improve the readability and clarity of the manuscript.

ORCID iDs

Michael A. Mischna https://orcid.org/0000-0002-8022-5319
David M. Kass https://orcid.org/0000-0002-7154-2566
Soumyo Dutta https://orcid.org/0000-0003-4840-6272
Scot Rafkin https://orcid.org/0000-0001-7464-1319
Daniel Tyler https://orcid.org/0000-0003-3845-3366
Stephen R. Lewis https://orcid.org/0000-0001-7237-6494
David Hinson https://orcid.org/0000-0002-1620-4011

References

Barnes, J. R., Haberle, R. M., Wilson, R. J., et al. 2017, in The Atmosphere and Climate of Mars, ed. R. M. Haberle et al. (Cambridge: Cambridge Univ. Press), 229
Bell, J. F., III, Wolff, M. J., & Malin, M. C. 2009, JGRE, 114, E08S92
Bertrand, T., Spiga, A., Rafkin, S., et al. 2013, In European Planetary Science Congress EPSC2013-545
Cantor, B. A., James, P. B., Caplinger, M., & Wolff, M. J. 2001, JGR, 106, 23653
Cantor, B. A., & Malin, M. C. 2002, Meteorological conditions at the MER landing sites, JPL Memorandum
Cantor, B. A., James, P. B., & Calvin, W. M. 2010, Icar, 208, 61
Cantor, B. A., Picket, N. B., Malin, M. C., et al. 2019, Icar, 321, 161
Chen, A., Cianciolo, A., Vasavada, A. R., et al. 2014, J. Spacecraft Rockets, 51, 1062
Christensen, P. R., Bandfield, J. L., Hamilton, V. E., et al. 2001, JGR, 106, 23,823
Cianciolo, A. D., Way, D. W., & Powell, R. W. 2008, in AIAA/AAS Astrodynamics Specialist Conf. and Exhibit (Reston, VA: AIAA), 6427
Colaïtis, A., Spiga, A., Hourdin, F., et al. 2013, JGRE, 118, 1468
Conrath, B. J., Pearl, J. C., Smith, M. D., et al. 2000, JGR, 105, 9509
Fenton, L., Reiss, D., Lemmon, M., et al. 2016, SSRv, 203, 89
Forget, F., Hourdin, F., Fournier, R., et al. 1999, JGR, 104, 24155
Formisano, V., Angrilli, F., Arnold, G., et al. 2005, P&SS, 53, 963
Golombek, M., Kass, D., Williams, N., et al. 2020, JGRE, 125, E06502
Guzewich, S. D., Newman, C. E., de la Torre Juárez, M., et al. 2016, Icar, 268, 37
Haberle, R. M., Pollack, J. B., Barnes, J. R., et al. 1993, JGR, 98, 3093
Haberle, R. M., Kahre, M. A., Hollingsworth, J. L., et al. 2019, Icar, 333, 130
Heavens, N. G., Richardson, M. I., Kleinböhl, A., et al. 2011a, JGRE, 116, E01007
Heavens, N. G., Richardson, M. I., Kleinböhl, A., et al. 2011b, JGRE, 116, E04003
Hess, S. L., Ryan, J. A., Tillman, J. E., Henry, R. M., & Leovy, C. B. 1980, GeoRL, 7, 197
Hinson, D. P., Asmar, S. W., Kahan, D. S., et al. 2014, Icar, 243, 91
Hinson, D. P., Simpson, R. A., Twicken, J. D., Tyler, G. L., & Flasar, F. M. 1999, JGR, 104, 26997
Hinson, D. P., Tyler, D., Lewis, S. R., et al. 2019, Icar, 326, 105
Holmes, J. A., Lewis, S. R., & Patel, M. R. 2020, P&SS, 188, 104962
Hong, S.-Y., & Pan, H.-L. 1996, MWRv, 124, 2322
Hourdin, F., Forget, F., & Talagrand, O. 1995, JGR, 100, 5501
Johnson, A., Aaron, S., Chang, J., et al. 2017, in Proc. AAS Guidance Navigation and Control Conference (AAS-17-038) (Breckenridge, CO: AAS), 0877036357
Johnson, A., et al. 2022, in SciTech Forum 2022 (San Diego, CA: AIAA)
Justh, H. L., & Justus, C. G. 2007, LPI Contribution, 1353, 3291
Karlgaard, C. D., Beck, R. E., O'Keefe, S. A., et al. 2009, in 41st AIAA Thermophysics Conf. (Reston, VA: AIAA), 3916
Karlgaard, C. D., Kutty, P., Schoenenberger, M., et al. 2014, J. Spacecraft and Rockets, 51, 1029
Karlgaard, C., & Tynis, J. 2019, Mars Phoenix EDL Trajectory and Atmosphere Reconstruction Using NewSTEP NASA/TM-2019-220282, https://ntrs.nasa.gov/api/citations/20190026499/downloads/20190026499.pdf
Karlgaard, C., Korzun, A., Schoenenberger, M., et al. 2021, JSpRo, 58, 865

Kleinböhl, A., Schofield, J. T., Kass, D. M., et al. 2009, JGRE, 114, 10006
Kleinböhl, A., Schofield, J. T., Abdou, W. A., Irwin, P. J., & de Kok, R. 2011, JQSRT, 112, 1568
Kleinböhl, A., Wilson, R. J., Kass, D., Schofield, J. T., & McCleese, D. J. 2013, GeoRL, 40, 1952
Kleinböhl, A., Friedson, A. J., & Schofield, J. T. 2017, JQSRT, 187, 511
Kleinböhl, A., Schofield, J. T., & Kass, D. M. 2018, in 42nd COSPAR Scientific Assembly (Pasadena, CA: COSPAR), B4.1-32-18
Kleinböhl, A., Spiga, A., Kass, D. M., et al. 2020, JGRE, 125, e06115
Lefèvre, F. 2004, JGR, 109, E07004
Lemoine, F. G., Smith, D. E., Rowlands, D. D., et al. 2001, JGR, 106, 23359
Lewis, S. R., & Barker, P. R. 2005, Adv. Space Res., 36, 2162
Lewis, S. R., Read, P. L., Conrath, B. J., Pearl, J. C., & Smith, M. D. 2007, Icar, 192, 327
Maddock, R. W., Dwyer-Cianciolo, A. M., Litton, D., & Zumwalt, C. H. 2020, in AIAA Scitech 2020 Forum (Reston, VA: AIAA), 1269
McCleese, D. J., Schofield, J. T., Taylor, F. W., et al. 2007, JGRE, 112, E05S06
Michaels, T. I., & Rafkin, S. C. R. 2008, JGRE, 113, E00A07
Mischna, M. A., Kass, D. M., Friedson, A. J., et al. 2008, LPI Contribution, 1447, 9091
Montabone, L., Forget, F., Millour, E., et al. 2015, Icar, 251, 65
Navarro, T., Madeleine, J.-B., Forget, F., et al. 2014, JGRE, 119, 1479
Newman, C. E., Lewis, S. R., Read, P. L., & Forget, F. 2002, JGRE, 107, 5123
Pätzold, M., Häusler, B., Tyler, G. L., et al. 2016, P&SS, 127, 44
Pla-García, J., Rafkin, S. C., Kahre, M., et al. 2016, Icar, 280, 103
Putzig, N. E., & Mellon, M. T. 2007, Icar, 191, 68
Rafkin, S. C., & Michaels, T. I. 2003, JGRE, 108, 8091
Rafkin, S. C. R., Michaels, T. I., & Haberle, R. M. 2004, GeoRL, 31, L01703
Rafkin, S., & Michaels, T. 2019, Atmos, 10, 747
Rafkin, S. C. R., Haberle, R. M., & Michaels, T. I. 2001, Icar, 151, 228
Rafkin, S., Pla-Garcia, J., & Leung, C. 2017, European Planetary Science Congress, EPSC2017-369
Read, P. L., & Lewis, S. R. 2004, The Martian Climate Revisited: Atmosphere and Environment of a Desert Planet (New York: Springer Praxis)
Read, P. L., Galperin, B., Larsen, S. E., et al. 2017, in The Atmosphere and Climate of Mars, ed. R. M. Haberle et al. (Cambridge: Cambridge Univ. Press), 172
Richardson, M. I., Toigo, A. D., & Newman, C. E. 2007, JGRE, 112, E09001
Rodriguez-Manfredi, J. A., de la Torre Juarez, M., et al. 2021, SSRv, 217, 48
Rosenblatt, P., Lainey, V., Le Maistre, S., et al. 2008, P&SS, 56, 1043
Smith, D., Neumann, G., Arvidson, R., Guinness, E., & Slavney, S. 2003, Mars Global Surveyor Laser Altimeter Mission Experiment Gridded Data Record, PDS record MGS-M-MOLA-5-MEGDR-L3-V1.0, NASA
Smith, M. D. 2004, Icar, 167, 148
Smith, M. D., Pearl, J. C., Conrath, B. J., & Christensen, P. R. 2000, JGR, 105, 9539
Spiga, A., Bourrier, V., Forget, F., et al. 2010a, in 40th International Conf. on Environmental Systems (Reston, VA: AIAA), 6284
Spiga, A., Forget, F., Lewis, S. R., & Hinson, D. P. 2010b, QJRMS, 136, 414
Tamppari, L. K., Barnes, J., Bonfiglio, E., et al. 2008, JGRE, 113, E00A20
Tyler, D., Jr., & Barnes, J. R. 2013, IJMSE, 8, 58
Tyler, D., Jr., & Barnes, J. R. 2014, Icar, 237, 388
Tyler, D., Jr., & Barnes, J. R. 2015, GeoRL, 42, 7343
Tyler, D., Jr., Barnes, J. R., & Haberle, R. M. 2002, JGRE, 107, 5018
Tyler, D., Jr., Barnes, J. R., & Skyllingstad, E. D. 2008, JGRE, 113, E00A12
Vasavada, A. R., Chen, A., Barnes, J. R., et al. 2012, SSRv, 170, 793
Wilson, R. J., & Hamilton, K. 1996, JAtS, 53, 1290
Zurek, R. W., & Smrekar, S. E. 2007, JGRE, 112, E05S01